Università degli Studi di Padova

Dipartimento di Matematica "Tullio Levi Civita"
Department of Information Engineering
Corso di Laurea Magistrale in Matematica

Analytical Study of Mixed-Mode Oscillations in Human β-Cells

Author
Simone Battaglin
1134451

Supervisor
Prof. Morten Gram
Pedersen

19th April 2019

Andrea. Era
Il ciliegio dove fu poi il solco.
Al piede la palla, agli occhi una piega
Sulle strade di casa manco da molto,
Muore il ricordo, non salgo la vetta
Di ieri. Alberto,
Nel rombo del vespro, appare
Ombra lontana, vicino sorriso
Alle strade del mondo, torno
Dove non so, la terra
Ripiomba.

Abstract
β-cells are specific cells located in pancreatic islets that produce and secrete insulin. The secretion of insulin happens as a consequence of a electrical activity: in the present thesis we analyse a mathematical model regulating that phenomenon. This model depends on eight variables, which are recognized having different time scales and hence classified as slow, medium or fast.
By varying some parameters of the model we remark the generation of mixed-mode oscillations: small amplitude oscillations with a global return mechanism. In order to explain it, a reduction of the model is performed and a 3d-model is obtained. The study of the singularities of this system let us notice the appearance of mathematical objects called *canards* in their neighborhood. The strong canard determines the funnel where simulations have to enter in order to begin oscillating around the weak canard. Finally secondary canards induce a discretization of the space and determine the number of small amplitude oscillations of the solution of the system.
We find good agreement between our analytical studies and numerical simulations.

Acknowledgements

Ringrazio il Professor Pedersen, per la molta pazienza che mi ha saputo accordare, per i tempi prolungati che mai ha giudicato, e per aver sempre trovato una parola positiva, di incitamento.

Ringrazio i miei genitori, per avermi permesso di seguire questo percorso, possibilità che non era per niente scontata, anche se spesso l'ho considerata tale. Per avermi sempre supportato e sopportato in questi anni, spronandomi a dare il meglio di me e capendo quando invece farsi da parte.

Ringrazio i miei amici tutti. Gli amici del collegio Murialdo, che si sono rivelati fin da subito al pari di veri fratelli. Gli amici di Matematica, con cui ho condiviso molte fatiche e molti esami, ma anche molti momenti di divertimento. Gli amici del Pollaio, con i quali ho praticamente convissuto in questi ultimi anni, con i quali sono cresciuto moltissimo e grazie ai quali ho imparato molto di più di quello che ti possa insegnare l'università.

Ringrazio infine i Professori incontrati durante questo lungo percorso, per avermi dimostrato che gli stereotipi sui docenti irraggiungibili e disumani non valgono all'interno del nostro bellissimo dipartimento di matematica, di cui andrò sempre fiero e conserverò sempre un bellissimo ricordo.

Contents

Abstract iii

Acknowledgements v

Contents 1

1 Introduction 3
- 1.1 Biological Preliminaries . . . 3
- 1.2 Structure of the Thesis . . . 6

2 Construction of the Model 9
- 2.1 Circuit Modelling of a Cell . . . 9
- 2.2 Parameters Setup . . . 12
  - 2.2.1 Calcium Channels . . . 13
  - 2.2.2 Potassium Channels . . . 14
  - 2.2.3 Sodium Channels . . . 16
  - 2.2.4 Leak Current . . . 16
  - 2.2.5 Final Statements . . . 16

3 Different Time Scales of the 8d-Model 19

4 Dynamics of the 8d-Model 21
- 4.1 Spiking Behaviour . . . 21
- 4.2 Stable Behaviour . . . 23
- 4.3 Bursting Behaviour . . . 24

5 Geometric Singular Perturbation Theory 27
- 5.1 3d-System . . . 28
- 5.2 Folded Singularities . . . 30
- 5.3 Canards . . . 33
- 5.4 Example: Van der Pol Equation . . . 35
- 5.5 Last Considerations . . . 38

6 Reduction to a 4d-Model 39
- 6.1 Resume of the Method . . . 39
- 6.2 Eigenvalue Analysis of the 8d-Model . . . 40
- 6.3 Variables Reduction . . . 44
- 6.4 4d-Model . . . 47

7 3d-Model **51**
7.1 Choice of the Model 51
7.2 Structure of the 3d-Model 52
7.3 Singular Canards 55
7.4 Maximal Canards 57

8 Conclusions **63**
8.1 Suggestion for Future Developments 64

Appendices **65**

Bibliography **75**

Chapter 1

Introduction

This thesis comes from my desire to work with biological applications of Mathematics that I hope will be part of my future job. Professor Pedersen gave me the opportunity to use a model that he constructed in 2010 in [1] to let me follow my aspiration; human pancreatic β-cells are modellized in it, regarding the process of insulin secretion.

Let us begin with a little introduction to the biological processes which are interesting to concretely understand what this model aims to study.

1.1 Biological Preliminaries

When stimulated by glucose arriving, pancreatic β-cells induce insuline production and secretion. Let us start by briefly explaining this process.

Insulin Production and Secretion

During the assimilation process of food, levels of glucose in the blood grow up; by consequence glucose methabolism of cells increases too and the overwhelming energy activate the ATP (Adenosine TriPhosphate) production. The increasing of the ATP/ADP ratio allows many ion channels to open and close causing a periodic polarisation and depolarisation of the cell, which causes, inversely, other ion channels to open or close. We will clarify in the following lines which channels play which roles during these operations. By the way, we can claim that the presence of Calcium in the cell will provoke the secretion of insulin.

Glucose methabolism stimulates also insulin gene transcription and mRNA translation on ribosome attached to the rough endoplasmic reticulum. Messenger-RNA connects amino acids into a a peptide chain called *preproinsulin* (the preprohormone related to insulin). This chain will be cut in the endoplasmic reticulum generating *proinsulin* and pass to the Golgi apparatus where it is put into membrane-bound vesicles which contain a set of glycosylation enzimes too. Thanks to them the prohormone will be cut in three active peptides and two of them, connected by disulfide bonds, will finally give birth to insulin. These vesicles unleash their contents in the extracellular space by calcium-triggered

exocitosis, as it was said before.[1]

Ion Channels Role

In this thesis we are firstly interested in modelling the secretion, and not the production, of insulin, so it will be useful to understand which channels take part in this process and how their activation works.[2]

- Potassium outward channels (K^+):
  - ATP-dependent K^+ channels, called K_{ATP} channels;
  - Delayed-rectifier K^+ channels, called K_V channels;
  - Large-conductance Ca^{2+}-activated K^+ channels, called BK channels.

  When open they let potassium *exits from* the cell by diffusion, otherwise they keep it inside against the differential of concentration. At the equilibrium state potassium channels are open. We will see that they have a peculiarity in our system which is that they do not inactivate.

- Human Ether-à-go-go-Related Genes channels, called hERG channels.

  They are K^+ channels too but they let pass an inward flow.

- Calcium channels (Ca^{2+}):
  - Transient T-type Ca^{2+} channels;
  - Long-lasting L-type Ca^{2+} channels;
  - P/Q-type Ca^{2+} channels.

  When open they let calcium *enters into* the cell, otherwise they keep it outside. At the equilibrium state they are all closed.

- Sodium channels (Na^+).

  They work exactly like Ca^{2+} channels.

We have to remember that, at rest, the interior of human β-cells has an electrical potential of about $-70\ mV$ with respect to extracellular fluid. When glucose enters the $\beta-$cell, increasing ATP provokes the closure of K_{ATP} channels and consequently a depolarization of the cell. T-type Ca^{2+} channels open at $-50\ mV$ and close at $-35\ mV$ and in the order L-type $(-40, -15\ mV)$ and P/Q-type $(-20, 0\ mV)$ do the same. Sodium channels contribute in depolarization too, opening at $-30\ mV$. As affirmed in [5], hERG channels intervene to sustain the process of spike-frequency adaptation and thus contribute to the control of burst duration and they play a role in depolarisation and repolarisation too. Finally K_V and BK calcium-dependent channels provoke the repolarisation of the cell.

[1] Everything written in these firsts paragraphs can be easily found in any manual of molecular biology. In particular I consulted [2].

[2] All data and functioning esplained in the following were found in Braun et al. [3]; Fall et al. [4].

Ion Channels Activity

I have used terms such as open, closed and inactivated to describe the state of channels. Still we do not know what it does really mean. Hence let us look to the ion channels configuration, trying to understand how it changes during the insulin secretion. This will be very usefull to better comprehend the model that we are going to construct in the next chapter.

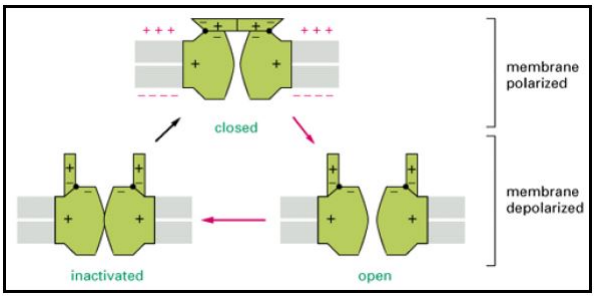

Figure 1.1: The figure was taken from [2]. It is quite self-explanatory, voltage-dependent channels can be in one of the represented state according to the phase of polarisation/depolarisation the cell is going through. In this particular case it is a Na^+-permeable channel. More in details, when the membrane is depolarized, the energy of the open conformation is lower and so the channel has a high probability of opening. But the free energy of the inactivated conformation is lower still, and so, after a randomly variable period spent in the open state, the channel becomes inactivated. Thus the open conformation corresponds to a metastable state that can exist only transiently. The red arrows indicate the sequence that follows a sudden depolarization, while the black arrow indicates the return to the original conformation as the lowest energy state after the membrane is repolarized.

First of all, not every channel has the same configuration at the same instant, even if they are selective for the same ion, and even if they are of the same type. That is why it will be interesting to consider the probability of a channel to be in a particular state (e.g. open), and therefore which percentage of channels is actually in that state. In fact, trying to describe every singular channel is not worthy, because of their great number: then a statistical approach is the only valuable one. Every voltage-dependent channel has to cycle among the following three states:

- closed
- open
- inactivated

For example, let us consider sodium channels shown in Figure 1.1. When the cell depolarizes, voltage gets to reach the threshold value at which most channels open, letting pass many ions. Hence sodium enters the cell, so electrical potential decreases even more. With these hypothesis we could think that the depolarisation will continue forever, since the voltage threshold to open is already passed. Something has to stop depolarisation, in order to allow this

methabolic process to happen only when it is necessary. Since the channels cannot close, they are inactivated when passing through a second threshold. Inactivation lasts for a sufficiently large time, called *refractory time*, in order to permit the repolarization. During the repolarization, the voltage crosses the first threshold again and forces channels to close back, restoring their initial state. When the refratory time has passed, the whole process will start again, allowing channels to reopen.

Calcium channels will behave the same way; potassium ones will work inversely, since these ions exit when channels are open.

The channels will follow the cycle *closed-open-inactivated*, "starting" (at $-70\ mV$) from the closed or the open state dependently on their rest position. This means that, roughly, at rest potassium (respectively sodium/calcium) channels are open (resp. closed): when membrane depolarization occurs they activate and they get closed (resp. open); by consequence depolarization accentuates until channels are inactivated, so that they cannot open again until this phase is terminated and potential is back to the initial value.

The last thing to understand is how a channel passes through these states. We can represent it quite simply by thinking to a channel as a tube with two doors: by looking to Figure 1.2 one of them controls the open and closed states (which will represents the activation gate in our model) while the other one controls the inactivation gate.

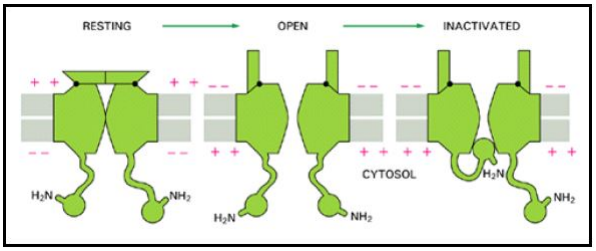

Figure 1.2: The figure was taken from [2]. It is "ball-and-chain" model of rapid inactivation for a voltage-gated K^+ channel, such as hERG channels in our model. When the membrane is depolarized, the channel opens and begins to conduct ions. The open channel is then susceptible to occlusion (inactivation) by the amino-terminal 19 amino acid "ball", which is linked to the channel proper by a segment of unfolded polypeptide chain that serves as the "chain". For simplicity, only two balls are shown; in fact there are four, one from each subunit. A similar mechanism, using a different segment of the polypeptide chain, is thought to operate in Na^+ and Ca^{2+} channels inactivation.

1.2 Structure of the Thesis

This short introduction clearly does not expect to be a comprehensive biological guide for the processes happening in human β-cells. It is simply intended to get the reader a little more familiar with these biological notations, in order to understand the functions of ionic channels, as long as causes and consequences of the flux through them. Hence, after this brief biological introduction, let us explain how our mathematical work will proceed.

In chapter 2 I will take into account a system of partial differential equations built by Pedersen in [1] based on data taken by molecular biologists and briefly justify this construction. So this chapter will let us make a connection between the biological subject previously introduced and its mathematical representation.

By studying a dimensionless version of the model, in chapter 3 we will notice that we are working with a multi-timescale system, where the electrical potential can be considered the fast variable of the system. Therefore this will justify further fast-slow analysis.

In chapter 4 I will analyse this 8-dimensional model by varying some of the parameters that appear in it and see how the electrical potential will assume one of the following behaviours: it can tend to a stable value; otherway it can stabilise to a periodic trend and this trend can presents spiking or bursting oscillations. These bursting oscillations are characterized by small impulses - or spikes - riding on top of an elevated voltage plateau [6]. From a biological point of view it is interesting to remark that Scott et al. verified that secretion of insulin is much more efficient during this last type of electrical activity [7].

Chapter 5 concerns general fast-slow analysis. The reader is introduced to canard-induced *Mixed Mode Oscillations* (MMO) theory. In this chapter I will also classify some types of singularities[3]: this will be fundamental to understand mathematical analysis of the 3d-model, obtained thanks to a reduction of its dimensions. I will give detailed explanations about canards in system with one fast variable and two slow variables, but more exhaustive informations about it can be found in [9; 10].

After that I am going to simplify the 8d-model by reducing its dimension, in chapter 6. To this end I will study the real parts of the eigenvalues of the jacobian relative to the system and observe that four of them are always negligibles. This will let us construct a four dimensional model, paying attention to which independent variables are better fitted to become dependent. Simulations will show that it respects quite well the characteristics of the initial system.

In chapter 7 I will choose a three dimensional model which will try to preserve to the best the behaviour of the previous 4d-model. This further reduction would seem forced, but it is due to another type of reasoning that can be done to variables with similar velocity. This reduction is performed in order to apply the previously mentioned canard-induced MMO theory. Other simulations will confirm that the different dynamics of the systems are still preserved even in the 3-dimensional model.

Remarking that the potential is a fast variable with respect to the other two, in chapter 5 I will study the 3d-model: I will be able to build the slow folded surface where the derivative of the fast variable will vanish and slow variables lead the flow. We will see how Small Amplitude Oscillations (SAO), which occur during bursting, are actually associated to the system crossing the folded surface near a folded singularity - therefore place on a fold line - and rotating around the weak canard. Conversely, Large Amplitude Oscillations (LAO) are associated to another crossing of the fold surface near the second fold line, allowing the global return mechanism to occur and solutions to close in periodic cycles.

Finally, a study on the number of SAOs and on the maximal canards will

[3] A more complete classification will be displayed in appendix B, following the work of Benoît [8].

allow us to claim there is a link between our model with its MMO dynamics and the canard theory, in the neighborhoor of the folded node we are going to find.

Chapter 2

Construction of the Model

The aim of this chapter is to construct a plausible model which may reprensent the temporal evolution of β-cell during insulin secretion. In order to do it, we will proceed through two steps:

- first of all we will think to the cell structure as a circuit, following the interpretation of Hodgkin and Huxley [11], Fall et al. [4] and others;
- after that we will set the parameters according to Pedersen [1] and Braun et al. [3].

2.1 Circuit Modelling of a Cell

I am going to resume the work made by Fall et al. to build a model which will describe cells as circuits, with membrane potentials, capacitors, resistances and voltage-dependent ion channels in the following paragraphs.

Interested readers can take a look to [4; 12] to find a full tractation of the model.

Potentials and Nernst Equation

First of all, the *electrical potential* through the cell membrane depends on intracellular and extracellular ion concentrations. The membrane allows some type of ion to cross through specific channels, sometimes by diffusion, so following the concentration gradient (which is a *chemical potential*), and sometime against this gradient, employing energy as it happens in sodium-potassium pump.

Let us consider whatever ion x. At the *equilibrium potential*, electrical and chemical forces are balanced so that there is no flow of x through the membrane. This is regulated by the *Nernst equation*, which is derived in [4] from the expression for the change in Gibbs free energy when one mole of an ion of valence z is moved across a membrane.

$$V_x = \frac{61.5}{z} Log_{10}\left(\frac{x_{out}}{x_{in}}\right) \tag{2.1}$$

Let's recall that the valence z is the charge of x (e.g. for Ca^{2+} $z = +2$). This potential is called *reversal potential* or *Nernst potential*. It is assumed that it is constant, for a given ion x.

Since all ions in this model have positive valence, looking to this formula we can understand that, Nernst potential V_x is positive when the outside concentration of x is greater than the inside one (i.e. when the gradient is pointing inside); otherwise it is negative. Reversal potential denotes the value of membrane potential V at which ion flow vanishes and it is measured in milliVolt $[mV]$, so basically it is the equilibrium potential for one permeant ion.

Membrane Electrical Behaviour

The model is then seen as an electrical circuit where the cell membrane is a capacitor, since phospholipid bilayer separates the ions on the inside from those on the ouside of the cell. In order to "translate" the electrical circuit diagram into ODEs, we use the traditional interpretation of each circuit element along with Kirchhoff's law and since the membrane acts as a capacitor, the capacitive current across the membrane can be written as:

$$I_{cap} = C\frac{\mathrm{d}V}{\mathrm{d}t}$$

Assuming that each ion channel is perfectly selective, the resulting potential of the whole cell is given as a weighted sum of Nernst potentials for each ion based on its conductance. Thanks to Ohm's law, current flows down a voltage gradient in proportion to the resistance in the circuit [4] and it can be expressed as:

$$I = \frac{V}{R} = gV$$

The current which passes through a channel will be denoted by I_x and the conductance of each ion channel by g_x. I remember to the reader that conductance g can be seen as the inverse of a resistance R since it represents the facility for a ion to pass through the channel that has a resistance.

Thanks to the previous formula and remembering that reversal potentials are supposed constant for each ion x, I can write:

$$I_x = -g_x(V - V_x)$$

where I chose a negative sign because positive charges are moving. Here $V - V_x$ represents the driving force across the membrane provided by the "ionic battery".

By resuming, we modelised the cell with a circuit where:

- phospholipid bilayer acts as a capacitor;
- ionic permeabilities of the membrane act as resistors;
- electrochemical driving forces act as batteries driving the ionic currents.

All of these ionic and capacitative currents are arranged in a parallel circuit, as shown in Figure 2.1.

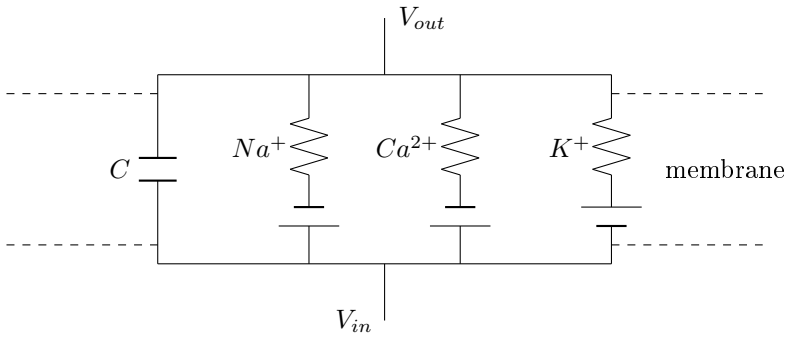

Figure 2.1: The equivalent electrical circuit for an electrically active membrane. The driving force for the ions is indicated by the symbol for the electromotive force (e.g. potassium enters the cell), which is given by the difference between the membrane potential $V = V_{in} - V_{out}$ and the Nernst potential.

Kirchhoff's law of charge conservation dictates that capacitative current must balance with ionic current, which implies that:

$$I_{cap} = \sum_x I_x$$

Finally we have:

$$C\frac{\mathrm{d}V}{\mathrm{d}t} = -\sum_x g_x(V - V_x)$$

Activation and Inactivation Gates

Channels can be thought to have gates that regulate the permeability of the pore to ions. Hodgkin and Huxley in [11] established experimentally that our gates are *voltage dependent*. Then channels can open and close depending on the membrane potential, and of course ions crossing the membrane through these same channels modify the membrane potential, so these variables are interdependents. Channels are time-dependent too, in the sense that there is a time delay which will slow down the respective variable.

All this can be modeled as differential equations where the fraction of open gates f_x is described by the general form:

$$\frac{\mathrm{d}f_x}{\mathrm{d}t} = \frac{f_x - f_{x,\infty}(V)}{\tau_x}$$

where $f_{x,\infty}(V)$ denotes the equilibrium state and τ_x is a time delay constant.

Then, we have to include this new relationship in the differential equation for membrane potential, since the conductance of channels surely depends on the fraction of open channels f_x.

Thus we will find:

$$C\frac{\mathrm{d}V}{\mathrm{d}t} = -\sum_x f_x g_x(V - V_x)$$

2.2 Parameters Setup

In 1952 Hodgkin and Huxley[1] showed that insulin secretion from β-cells is related to the electrical activity through the cell membrane and they thought a mathematical model which respected this fact. Many models have been presented starting from this first one: as announced in the introduction of this work, we will consider the model constructed by Pedersen in [1].

As I said before membrane potential is our first variable and it is derived by using Ohm's law:

$$\frac{\mathrm{d}V}{\mathrm{d}t} = -I_{Total} \tag{2.2}$$

where each current has been divided by the membrane capacitance (estimated at nearly 9.9 pF according to [1]) - such that currents are measured in picoAmpère on picoFarad $[pA/pF]$ - and where:

$$I_{Total} = (I_{K_V} + I_{BK} + I_{hERG} + I_{CaT} + I_{CaL} + I_{CaPQ} + I_{Na} + I_{leak})$$

Each ion channel treated here activates at a certain equilibrium voltage, so it let pass the ion for which it is sensible. After that, it is inactivated in order to let repolarise the cell, and a caracteristic refractory time prevents it to reopen before repolarisation. So for each channel of a specific ion x I indicate with m_x the fraction of activated open channels and with $1 - h_x$ the fraction of inactivated channels.[2] Then ion currents I_x can be rearranged like it follows:

$$I_x = g_x m_x h_x \left(V - V_x\right) \tag{2.3}$$

where g has been divided by the membrane capacitance, such as current, and is so measured in nanoSiemens on picoFarad $[nS/pF]$.

Hence m and h belong to the interval $[0, 1]$: some channels are assumed not to inactivate (which means that $h_x = 1$) some to activate instantaneously ($m_x = m_{x,\infty}$), but in general activation m_x and inactivation h_x are supposed to follow the first-order equations:

$$\begin{aligned} \frac{\mathrm{d}m_x}{\mathrm{d}t} &= \frac{m_{x,\infty}(V) - m_x}{\tau_{mx}} \\ \frac{\mathrm{d}h_x}{\mathrm{d}t} &= \frac{h_{x,\infty}(V) - h_x}{\tau_{hx}} \end{aligned} \tag{2.4}$$

where τ is a *time-constant of activation/inactivation* and $m_{x,\infty}$ (respectively $h_{x,\infty}$) is the *steady-state* voltage-dependent activation (respectively inactivation) *function* of the current.

As we cannot distinguish and count every channel in a deterministic way, it is suitable to follow a statistical approach and suppose that these steady-state functions are described with Boltzmann functions:

$$\begin{aligned} m_{x,\infty}(V) &= \frac{1}{1 + \exp\frac{V - V_{mx}}{n_{mx}}} \\ h_{x,\infty}(V) &= \frac{1}{1 + \exp\frac{V - V_{hx}}{n_{hx}}} \end{aligned} \tag{2.5}$$

[1] See [11].

[2] Remember ions state classification seen in the first chapter.

The *slope parameter* n is negative for steady-state activation functions, positive for inactivation ones. At the beginning Nernst potential is greater than the rest state potential (nearly $-70\ mV$ as I wrote before), so $V - V_f < 0$: then the sign of this slope parameters leads that, at that moment, really a few channels are open (since $0 < m \ll 1$) and very few channels are inactivated too ($0 < 1 - h \ll 1$).

Let's describe mathematically each of these channels.

2.2.1 Calcium Channels

As stated in the preambule to this section, calcium influx through its channels generates a current that can be expressed like:

$$\begin{aligned} I_{CaT} &= g_{CaT}\ m_{CaT}\ h_{CaT}\ (V - V_{CaT}) \\ I_{CaL} &= g_{CaL}\ m_{CaL}\ h_{CaL}\ (V - V_{CaL}) \\ I_{CaPQ} &= g_{CaPQ}\ m_{CaPQ}\ (V - V_{CaPQ}) \end{aligned} \tag{2.6}$$

The total calcium current activates rapidly (in less than $1ms$): it is then assumed that all calcium channels activate instantaneously. Therefore, the activation function is simply given by the steady-state activation function:

$$\begin{aligned} m_{CaT} &= m_{CaT,\infty}(V) = \left(1 + \exp\frac{V - V_{mCaT}}{n_{mCaT}}\right)^{-1} \\ m_{CaL} &= m_{CaL,\infty}(V) = \left(1 + \exp\frac{V - V_{mCaL}}{n_{mCaL}}\right)^{-1} \\ m_{CaPQ} &= m_{CaPQ,\infty}(V) = \left(1 + \exp\frac{V - V_{mCaPQ}}{n_{mCaPQ}}\right)^{-1} \end{aligned} \tag{2.7}$$

The low-voltage T-type channels contribute to the depolarisation of the membrane and were found to inactivate faster than the L- and P/Q-type. This means that they are responsible for the fastest componenent of total calcium current inactivation, that acts with a time constant of $\tau_{hCaT} = 7ms$.

The high-voltage P/Q-type channels are assumed not to inactivate because they need a long time, which overcomes action potentials duration.

Finally high-voltage L-type channels inactivate with a time constant of $\tau_{hCaL} = 20ms$.

Their inactivation is given by the differential equation introduced before:

$$\begin{aligned} \frac{\mathrm{d}h_{CaT}}{\mathrm{d}t} &= \frac{h_{CaT,\infty}(V) - h_{CaT}}{\tau_{hCaT}} \\ \frac{\mathrm{d}h_{CaL}}{\mathrm{d}t} &= \frac{h_{CaL,\infty}(V) - h_{CaL}}{\tau_{hCaL}} \end{aligned} \tag{2.8}$$

where

$$\begin{aligned} h_{CaT,\infty}(V) &= \left(1 + \exp\frac{V - V_{hCaT}}{n_{hCaT}}\right)^{-1} \\ h_{CaL,\infty}(V) &= \max\left(0, \min\left(1, 1 + \frac{m_{CaL,\infty}(V)\ (V - V_{Ca})}{\Phi}\right)\right) \end{aligned} \tag{2.9}$$

where $\Phi = 57\ mV$ is a normalisation factor and $\max - \min$ have to appear just to confine h_{CaL} to the interval $[0, 1]$.

This choice is justified since inactivation function of the total calcium currents showed a U-shaped voltage dependence with maximal inactivation at $-10\ mV$: but we also know that P/Q-type do not inactivate and that T-type inactivate much earlier (about $-35mV$). So we can think that the U-shaped inactivation function reflects inactivation of the only L-type Ca^{2+} current. The amount of inactivated channels $(1 - h_{CaL,\infty})$ is finally assumed to be proportional to the activated L-type Ca^{2+} current: $m_{CaL,\infty}(V)\ (V - V_{Ca})$.

2.2.2 Potassium Channels

As we know, potassium channels are responsible for the outflux of K^+: at rest state they are open. When voltage-dependent potassium channels activate they get closed and after inactivation they keep closed, without the possibility of getting opened before a refractory time has passed.

$\mathbf{K_{ATP}}$ Channels

First of all, ATP-sensitive potassium channels are obviously the very first channel that activate; then the current they generate do not depend on percentage of activated or inactivated channels but just on intracellular ATP concentration, because they are not voltage-dependent:

$$I_{K(ATP)} = g_{K(ATP)}\ (V - V_K) \tag{2.10}$$

$\mathbf{K_V}$ Channels

The delayed rectifying potassium channels were assumed to activate on a voltage-dependent timescale[3]:

$$\tau_{mKV} = \begin{cases} \tau_{mKV,0} + 10 \exp\left(\min\left(Log_e(3), -\frac{V+20\,mV}{6\,mV}\right)\right) & \text{if } V < 26.6\ mV \\ \tau_{mKV,0} + 30\ ms & \text{otherwise} \end{cases} \tag{2.11}$$

We will assume that K_V channels do not to inactivate because of its slow inactivation kinetics (on the order of seconds). Then:

$$I_{K_V} = g_{K_V}\ m_{K_V}\ (V - V_K) \tag{2.12}$$

$$\frac{\mathrm{d}m_{K_V}}{\mathrm{d}t} = \frac{m_{K_V,\infty}(V) - m_{K_V}}{\tau_{mKV}(V)}$$

where

$$m_{K_V,\infty}(V) = \left(1 + \exp\left(\frac{V - V_{mKV}}{n_{mKV}}\right)\right)^{-1}$$

[3] In appendix C I performed a brief study of this function in order to better understand the velocity of m_{KV}, as it will be clarified in chapter 6.

BK Channels

Unlike other voltage-dependent channels, BK channels are controlled by Ca^{2+} influx too. Calcium also triggers vesicles exocytosis and that is why BK channels are fundamental in rapid repolarisation after this phenomenon. They are also assumed not to inactivate (i.e. $h_{BK} = 1$) since BK currents rapidly repolarize the membrane potential, while activation is given by the usual formula:

$$\frac{\mathrm{d}m_{BK}}{\mathrm{d}t} = \frac{m_{BK,\infty}(V) - m_{BK}}{\tau_{mBK}(V)} \tag{2.13}$$

where

$$m_{BK,\infty}(V) = \left(1 + \exp\left(\frac{V - V_{mBK}}{n_{mBK}}\right)\right)^{-1} \tag{2.14}$$

Since BK channels depends on calcium, we assume that the microdomain Ca^{2+} concentration is proportional to the total Ca^{2+} current:

$$I_{Ca} = I_{CaT} + I_{CaL} + I_{CaPQ}$$

Thanks to this, the steady-state function for BK channels is therefore assumed to depend not on V only but to be proportional to $-I_{Ca}(V) + B_{BK}$ too, where B_{BK} denotes basal, Ca^{2+}-independent but voltage-dependent activation.

Finally we can deduct the expression for BK current:

$$I_{BK} = (-I_{Ca}(V) + B_{BK})\, \bar{g}_{BK}\, m_{BK}\, (V - V_{BK}) \tag{2.15}$$

hERG Channels

They are K^+ channels too but they let pass an inward flow: Riz et al. considered them in their model since Rosati et al. proved that the inwardly rectified current, that these channels generate, help in depolarization and repolarization and that they may even sustain a process of spike-frequency adaptation and thus contribute to the control of burst duration [13; 5].

Parameters of the steady-state activation and inactivation functions which are used here were calculated by Rosati et al. too.

This current has the classical form:

$$I_{hERG} = g_{hERG}\, m_{hERG}\, h_{hERG}\, (V - V_{hERG}) \tag{2.16}$$

where

$$\begin{aligned}
\frac{\mathrm{d}}{\mathrm{d}t} m_{hERG} &= \frac{m_{hERG,\infty}(V) - m_{hERG}}{\tau_{mhERG}} \\
m_{hERG,\infty} &= \left(1 + \exp\left(\frac{V - V_{mhERG}}{n_{mhERG}}\right)\right)^{-1} \\
\frac{\mathrm{d}}{\mathrm{d}t} h_{hERG} &= \frac{h_{hERG,\infty}(V) - h_{hERG}}{\tau_{hhERG}} \\
h_{hERG,\infty} &= \left(1 + \exp\left(\frac{V - V_{hhERG}}{n_{hhERG}}\right)\right)^{-1}
\end{aligned}$$

2.2.3 Sodium Channels

Sodium channels contribute to the repolarisation of the cell.

Just as calcium channels, their activation is immediate, so the activation function is given by the steady-state activation function:

$$m_{Na} = m_{Na,\infty}(V) = \left(1 + \exp\left(\frac{V - V_{mNa}}{n_{mNa}}\right)\right)^{-1}$$

Inactivation function follows the standard differential equation:

$$\frac{\mathrm{d}h_{Na}}{\mathrm{d}t} = \frac{h_{Na,\infty}(V) - h_{Na}}{\tau_{hNa}}$$

where

$$h_{Na,\infty}(V) = \left(1 + \exp\left(\frac{V - V_{hNa}}{n_{hNa}}\right)\right)^{-1}$$

2.2.4 Leak Current

The leak current summarizes all currents not modelled explicitly, such as currents mediated by exchangers, pumps, chloride channels, nonselective channels, non-voltage-dependent cation channels.

It is simply expressed as:

$$I_{leak} = g_{leak}\ (V - V_{leak}) \tag{2.17}$$

2.2.5 Final Statements

The model presented in this chapter consists at last in a system of eight non-linear differential equations with three kinds of variables: the membrane potential V, activation functions m_x and inactivation functions h_x. Starting from now I will call it *the 8d-model*.

Default values of the parameters are given in Table 2.1: they were gathered by Pedersen in [1], where the reader can find any reference. Ion channels were identified using *Polymerase Chain Reaction*; specific blockers, targeted for each ion channel, made possible to investigate the reaction in insulin secretion from β-cells and to understand which channels play a role during this process[4].

I remind the reader that the operational sign in front of each Nernst potential ($V_K, V_{Ca}, V_{Na}, V_{leak}$) denotes the direction of the ion current as we remarked in 2.1.

Potential activation of singular channel represents the estimated potential at which half of the gates, of that type, are open: as we said in the introduction we have, in order, Ca^{2+} T-type ($-40\ mV$), K^+ hERG ($-30\ mV$), L-type ($-25\ mV$), Na^+ ($-18\ mV$) and P/Q-type ($-10\ mV$). Insulin is released as the membrane reaches the maximum potential, activating BK and K_V channels at ($0\ mV$) and hERG channels too, since they do not inactivate before ($-42\ mV$).

Finally we have to notice that time constants τ influence directly the time lapse before the reactivation of a channel. Concretely, our values vary between

[4] See [3].

2 ms and 100 ms; if $\tau < 2\ ms$ we can assume that the process happens instantaneously, the more τ increases and the more this delay increases too. We will better understand this phenomenon in the next chapter.

Param	Value	U.M.	Param	Value	U.M.	Param	Value	U.M.
V_K	-75	mV	$g_{K(ATP)}$	0.015	nS/pF	τ_{mBK}	2	ms
V_{Ca}	-65	mV	g_{CaT}	0.050	nS/pF	τ_{mhERG}	100	ms
V_{Na}	70	mV	g_{CaL}	0.140	nS/pF	τ_{hhERG}	50	ms
V_{mCaT}	-40	mV	g_{CaPQ}	0.170	nS/pF	n_{mCaT}	-4	mV
V_{hCaT}	-64	mV	g_{Na}	0.400	nS/pF	n_{hCaT}	8	mV
V_{mCaL}	-25	mV	g_{KV}	1.000	nS/pF	n_{mCaL}	-6	mV
V_{mCaPQ}	-10	mV	$\bar{g}_{BK}$	0.020	nS/pA	n_{mKV}	-10	mV
V_{mNa}	-18	mV	B_{BK}	20	pA/pF	n_{mBK}	-10	mV
V_{hNa}	-42	mV	g_{hERG}	0.200	nS/pF	n_{mNa}	-5	mV
V_{mKV}	0	mV	g_{leak}	0.015	nS/pF	n_{hNa}	6	mV
V_{mBK}	0	mV	τ_{hCaT}	7	ms	n_{mhERG}	-10	mV
V_{mhERG}	-30	mV	τ_{hCaL}	20	ms	n_{hhERG}	17.5	mV
V_{hhERG}	-42	mV	τ_{hNa}	2	ms			
V_{leak}	-30	mV	$\tau_{mKV,0}$	2	ms			

Table 2.1: Parameters gathered by Pedersen in [1]

Chapter 3

Different Time Scales of the 8d-Model

Scaled time will be very usefull in the following chapters, when they will let us approximates faster and slower variables in different ways. For now let us understand which variables are faster and which ones are slower.

In the previous chapter we claimed that a bigger τ_x causes a bigger delay to the associated (in)activation variable (h_x) m_x. We can understand why this happens by rescaling the quantities into every equation of the 8d-model to obtain a dimensionless model, following the idea of Vo et al. in [6].

First of all, we can rewrite equations 2.2 and 2.3 into a single equation:

$$\frac{\mathrm{d}V}{\mathrm{d}t} = \sum_x g_x \, m_x \, h_x \, (V - V_x) \tag{3.1}$$

and do the same thing for one of the equations in 2.4 and 2.5:

$$\frac{\mathrm{d}m_x}{\mathrm{d}t} = \frac{1}{\tau_{mx}} \left(\left(1 + \exp \frac{V - V_{m_x}}{n_{mx}} \right)^{-1} - m_x \right) \tag{3.2}$$

We do not need to do the same for the inactivation function h_x since formulas are nearly identical.

To nondimensionalize the 8d-model I will introduce the following dimensionless variables and parameters, denoted by a hat:

$$\hat{V} = \frac{V}{V_{max}} \quad , \quad \hat{V_x} = \frac{V_x}{V_{max}} \quad , \quad \hat{t} = \frac{t}{t_{max}} \quad , \quad \hat{g}_x = \frac{g_x}{g_{max}} \quad , \quad \hat{n}_x = \frac{n_x}{V_{max}}$$

where

$$\begin{aligned} V_{max} &= \max \left(|V_K| , |V_{Ca}| , |V_{Na}| , |V_{mCaT}| , \dots \right) = 75 \; mV \\ t_{max} &= \max \left(\tau_{hCaT}, \tau_{hCaL}, \tau_{hNa}, \tau_{mBK}, \dots \right) = 100 \; ms \\ g_{max} &= \max \left(g_{K(ATP)}, g_{CaT}, g_{CaL}, g_{KV}, \dots \right) = 1 \; nS/pF \end{aligned}$$

We can easily substitute the expressions just found into 3.1 and 3.2 to calculate the equation of the dimensionless model:

$$\begin{aligned}
\frac{\mathrm{d}\hat{V}}{\mathrm{d}\hat{t}} &= t_{max}\, g_{max} \sum_x \hat{g}_x\, m_x\, h_x\, (\hat{V} - \hat{V}_x) \\
\frac{\mathrm{d}m_x}{\mathrm{d}\hat{t}} &= \frac{t_{max}}{\tau_{mx}} \left(\left(1 + \exp \frac{\hat{V} - \hat{V}_{mx}}{\hat{n}_{mx}} \right)^{-1} - m_x \right)
\end{aligned} \tag{3.3}$$

If we make a comparison between the reciprocals of the constants which are acting in the two equations we can see that:

$$\begin{aligned}
\delta_x &:= \frac{\tau_x}{t_{max}} \in [0.02, 1] \\
\epsilon &:= \frac{1}{t_{max}\, g_{max}} = 0.01
\end{aligned} \tag{3.4}$$

And replacing them into the dimensionless system 3.3 we have:

$$\begin{aligned}
\epsilon \frac{\mathrm{d}\hat{V}}{\mathrm{d}\hat{t}} &= \sum_x \hat{g}_x\, m_x\, h_x\, (\hat{V} - \hat{V}_x) \\
\delta_x \frac{\mathrm{d}m_x}{\mathrm{d}\hat{t}} &= \left(1 + \exp \frac{\hat{V} - \hat{V}_{mx}}{\hat{n}_{mx}} \right)^{-1} - m_x
\end{aligned} \tag{3.5}$$

This implies that, as τ_x increase, the associated (in)activation variable becomes slower because of the increasing of δ_x; and also that V is twice faster than the fastest among the other variables.

These observations will be usefull when I will study the 3d-system with the slow-fast analisys method. It is important to remark that in the following pages the parameter g_{KV} will be changed and will take values in $[0.05, 1.6]$ and of course this will cause a variation of g_{max} and ϵ too. Precisely, we will have $\epsilon = 0.025 > 0.02$: this will not be a problem since in the 3d-model I will choose not to keep the fastest variables among the remaining seven, so δ_x will be containend into the interval $[0.2, 1]$ and V will still be the fastest variable, as needed for the analisys.

Chapter 4

Dynamics of the 8d-Model

In this chapter I will study the behaviour of the 8d-model built in chapter 2: different types of dynamics of the model will be pointed out by changing the parameter g_{KV} from the default value and running the simulation. The importance of this parameter influencing the dynamics of the model was shown in [1]. From a biological point of view, increasing g_{KV} means to let pass a greater flow through the K_V-selective channels of the membrane; conversely reducing it means to reduce that flow as well.

Simulations were computed using *Wolfram Mathematica language* and all notebooks can be furnished to the reader by contacting the author.

In order to let the system start with all channels neither activated nor inactivated, I fixed initial conditions to:

$$(V, h_{CaT}, h_{CaL}, h_{Na}, m_{BK}, m_{KV}, m_{hERG}, h_{hERG}) = (-49\ mV, 1, 1, 1, 0, 0, 0, 1)$$

This choice will not really influence the study since waiting enough time solutions will stabilize around limit cycles or to an equilibrium.

Finally, I chose to plot the simulations starting from $t = 10^5\ ms$, to be sure that the model reached a stable configuration.

4.1 Spiking Behaviour

The first simulation is plotted in Figure 4.2 using default parameters of Table 2.1. It exhibits spiking solution for the membrane potential V as it can be seen in the first graphic of the image: it oscillates from $-67.9\ mV$, when the cell is totally polarized, to $-8.45\ mV$, during the maximal depolarization.

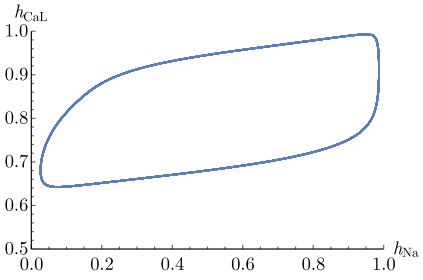

Figure 4.1: Simulation of h_{CaL} with respect to h_{Na} with default values of parameters indicated in Table 2.1.

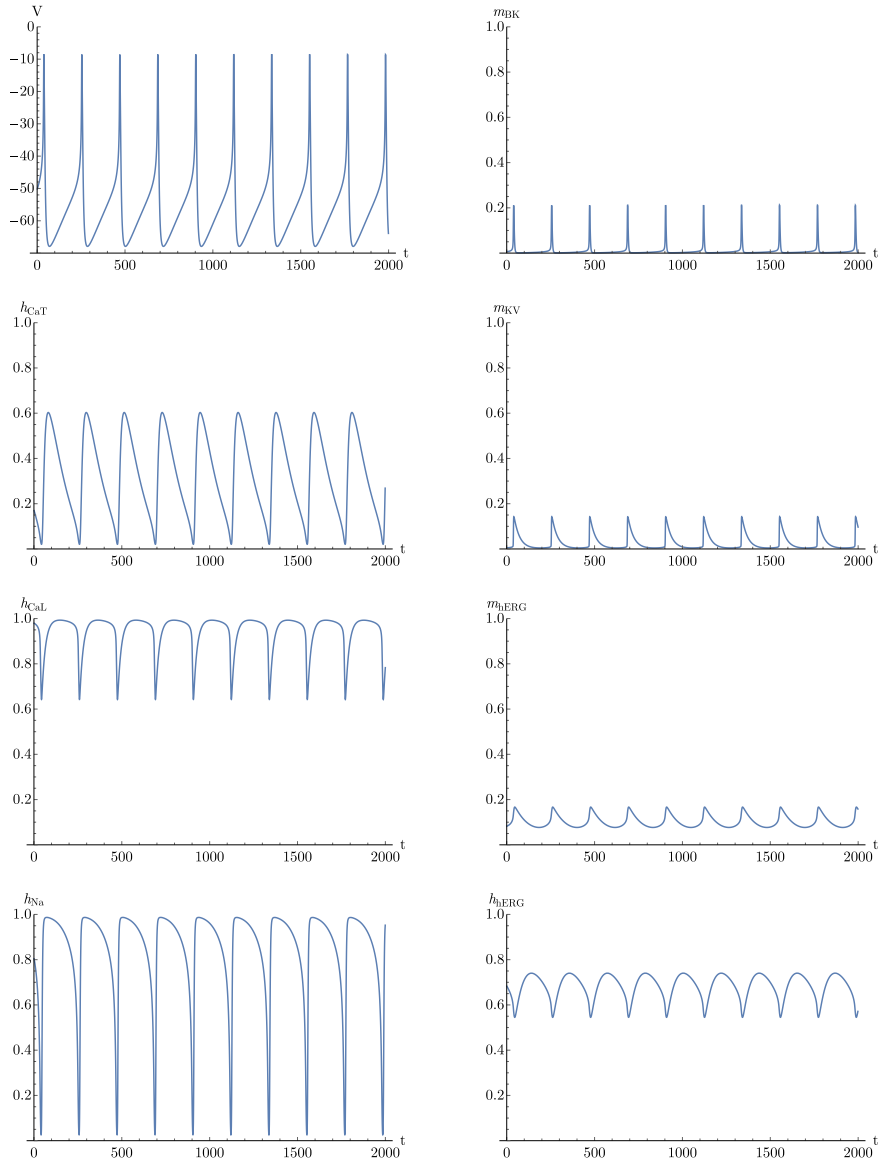

Figure 4.2: Simulations of $V, h_{CaT}, h_{CaL}, h_{Na}, m_{BK}, m_{KV}, m_{hERG}, h_{hERG}$ with default values of parameters indicated in Table 2.1.

As activation gates open and inactivation gates close during the temporal evolution, the system is pushed to spike when most of them change of configuration.

Even more, all variables seems to be periodic with the same period (frequency of 4.63 Hz); so plotting the simulation in the $xy-$plane with x and y whatever of the eight variables of the model, we will incur in a limit cycle. See for example Figure 4.1.

We can remark that h_{hERG} and, in particular, m_{hERG} have spikes less steep than the other ones, which means that they have a smaller reaction to rapid

changes. As stated in the previous chapter, this shows concretely that m_{hERG} and h_{hERG} are slower than the other variables in the system.

4.2 Stable Behaviour

By reducing g_{KV} from 1 nS/pF to 0.05 nS/pF we can see that a stable solution appear (Figure 4.3). We can also remark that same would happen with $g_{KV} = 1.6nS/pF$.

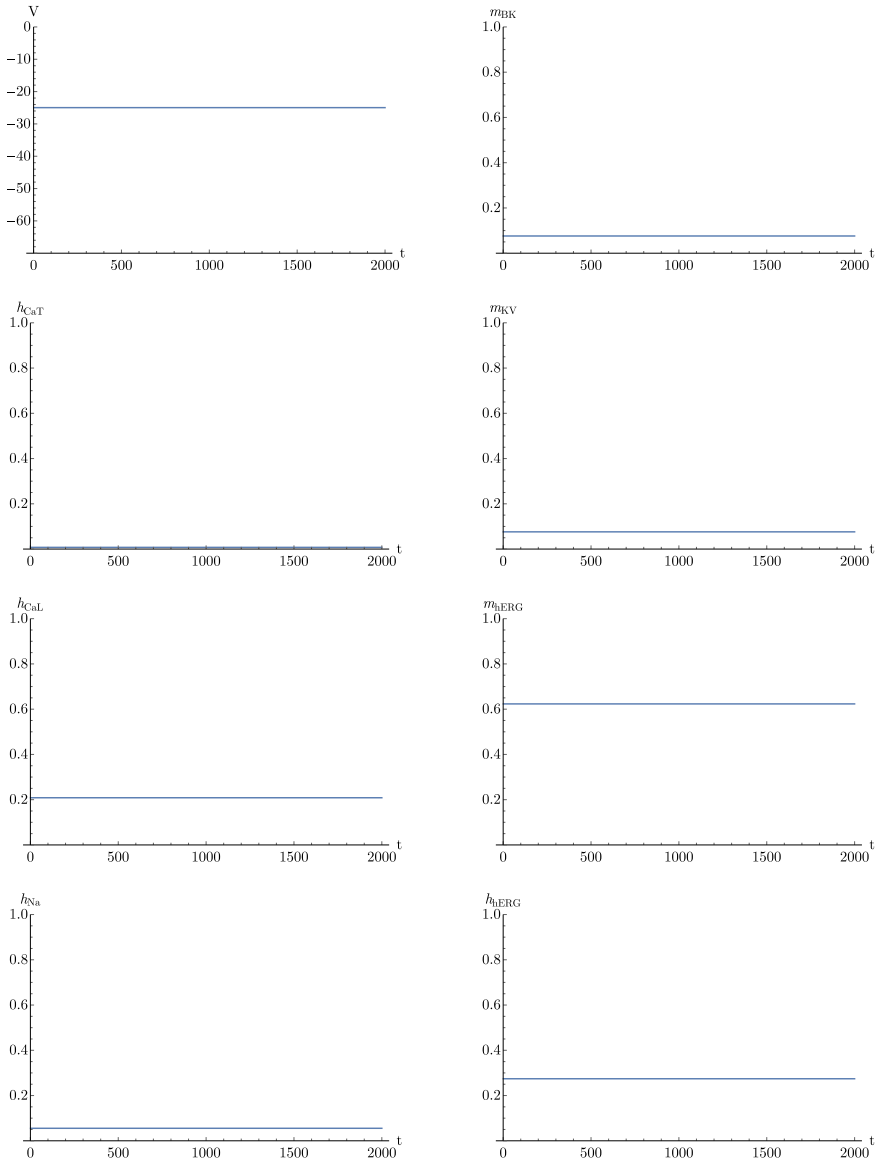

Figure 4.3: Simulations of $V, h_{CaT}, h_{CaL}, h_{Na}, m_{BK}, m_{KV}, m_{hERG}, h_{hERG}$ with default values of parameters indicated in Table 2.1 and $g_{KV} = 0.05\ nS/pF$.

4.3 Bursting Behaviour

The last type of solutions is even the most interesting one: by choosing $g_{KV} = 0.2\ nS/pF$, for example, we can see bursting oscillations of the voltage potential

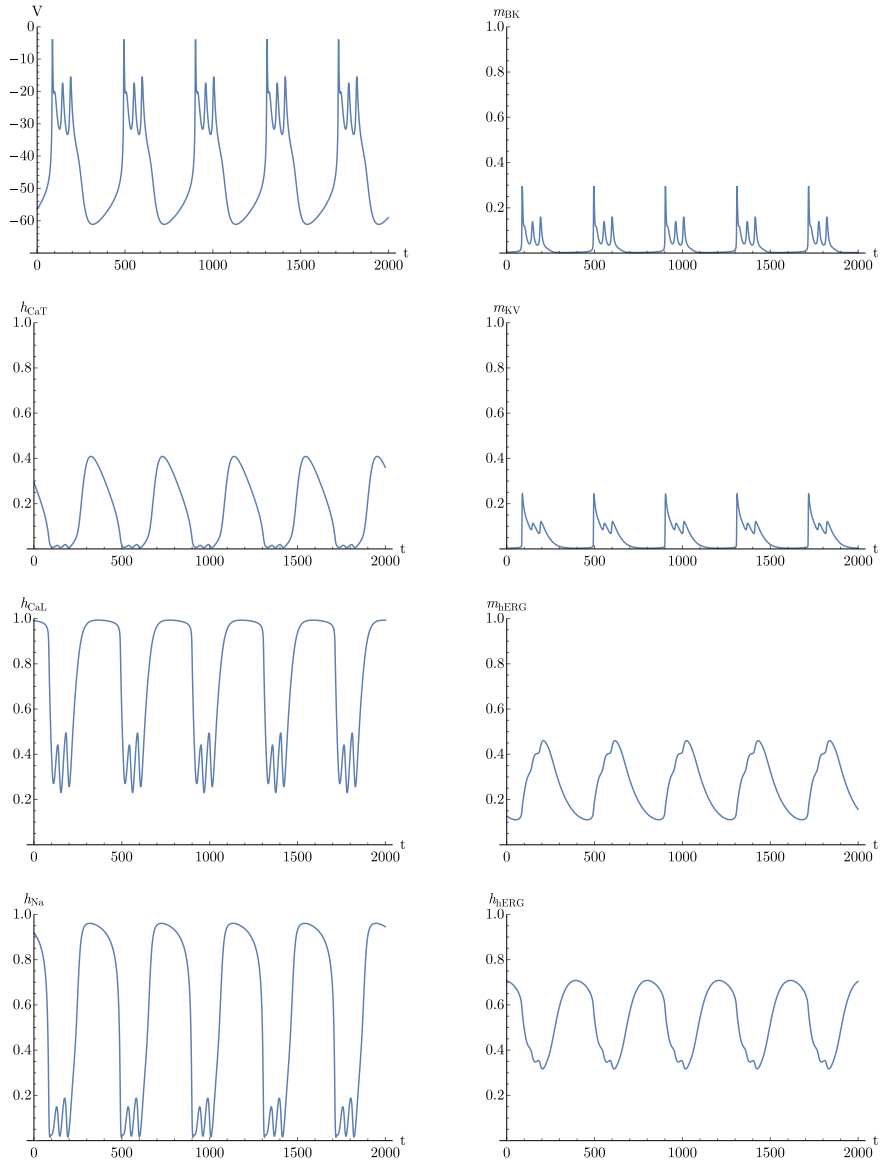

Figure 4.4: Simulations of $V, h_{CaT}, h_{CaL}, h_{Na}, m_{BK}, m_{KV}, m_{hERG}, h_{hERG}$ with default values of parameters indicated in Table 2.1 and $g_{KV} = 0.2\ nS/pF$.

As stated before, bursting is an interesting phenomenon since molecular biologists revealed an amelioration on insulin secretion when the membrane potential behaves that way [7].

Thanks to calculations made in chapter 3, the reduction of g_{KV} (and so of

g_{max}) reduces the velocity of V and not that of the other variables. Yet, ϵ will reach the value of 0.025 at most, remaining a fast variable.

This time we can see that voltage potential oscillates from $-61.1\ mV$, when the membrane is polarized, to $-3.95\ mV$, when it is depolarized. Variables are obviously still periodics but the presence of the bursting phenomenon increased the period: in fact frequency is reduced to $2.46\ Hz$.

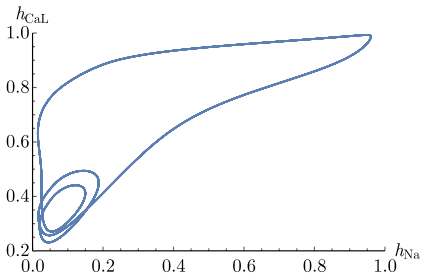

Figure 4.5: Simulation of h_{CaL} with respect to h_{Na} with default values of parameters indicated in Table 2.1 and $g_{KV} = 0.2\ nS/pF$.

Aiming to respect the parallelism with the spiking behaviour I decided to show the same limit cycle seen in Figure 4.1 for the bursting case too: in Figure 4.5 we can remark that small oscillations appeared in this new limit cycle.

In the next chapters, our analysis will aim to understand the genesis, the behaviour and the main characteristics of these oscillations related to our model. But first of all, let us talk of the theory that will permit that analysis in chapter 5.

Chapter 5

Geometric Singular Perturbation Theory

In chapter 3 we have seen that the 8d-model consists of variables with different time scales. This suggests that *Geometric Singular Perturbation Theory* (GSPT) could be a powerful tool to help us analysing our model. Before doing that I will dedicate this chapter to expose this theory and introduce the reader to concepts like *Mixed Mode Oscillations* (MMOs) and *Canard Theory*. Desroches et al. published a general work [9] on this subject, explaining MMOs for slow-fast systems. An important reference concerning specifically canard-generated MMOs is [10].

We refer to MMOs as complex patterns that arise in dynamical systems, in which oscillations with different amplitudes are interspersed: in fact oscillations are created by different mechanisms and their amplitude may have variations.

Historically, MMOs have first been observed in chemical reactions and discovered in 1970s with the Belousov-Zhabotinsky (BZ) reaction [14].

As suggested by their names, MMOs consist of a periodic series of oscillations: a number s of Small Amplitude Oscillations (SAO) alternated with a number L of Large Amplitude Oscillations (LAO). The notation to represent such an MMO is L^s. In this work we will always have $L = 1$.

The mathematical modeling of systems where MMOs occur result in nonlinear ordinary or partial differential equations and there are several mechanisms which can produce MMOs. One can find a list of those mechanisms in [15] made by Brøns et al.. In order to understand our model we are interested in canard-generated MMOs. They were first discovered in Van der Pol equation and they consist of a limit cycle - born in a Hopf bifurcation - that experiences the transition from a small, almost harmonic, cycle to a large relaxation oscillation. This transition, also called *canard explosion*, occurs through a sequence of intermediate limit cycles, called *canards cycles*, which can be asymptotically stable but still very hard to be observed in experiment or simulation because of sensitivity to the control parameter and, of course, to noise too. A representation of this phenomenon is shown in Figure 5.4: a small cycle is shown in (b), relaxation oscillations are periodic orbits that alternate between epochs of slow and fast motion (d), during the canard explosion in (c) we find an unstable

canard, born in a Hopf bifurcation.[1]

If we want to understand canard explosion, it is very important to consider the trajectory called *maximal canard*: it follows a slow manifold for a substantial time and distance from its stable to its unstable part, passing through a bifurcation. As we already said, this may happen only in the vicinity of a Hopf bifurcation.

In fact, in 2d-systems maximal canards occur for discrete values of the control parameter [16], but in 3d maximal canards are robust and are therefore persistent under small parameter changes [17].

Canards were first recognized and named by Benoît ([18; 8]). A group of French mathematicians of Strasbourg used nonstandard analysis to study slow-fast systems and figured out the existence of such elements. One can find a complete dissertation of nonstandard analysis in [19].

After having considered this approach, in order to study canards, I decided to follow the geometric approach of GSPT – also called *Fenichel Theory* – based on the works of Brøns et al. [10], Szmolyan and Wechselberger [20], Wechselberger [21] and, of course, Fenichel [22].

5.1 3d-System

In this section we will construct and study a generic 3d-system following mainly [9; 23].

We consider the three-dimensional fast-slow system of singularly perturbed ordinary differential equations in standard form:

$$\begin{aligned} \epsilon\dot{x} &= f(x,y,z) \\ \dot{y} &= g_1(x,y,z) \\ \dot{z} &= g_2(x,y,z) \end{aligned} \tag{5.1}$$

with f, g_1, g_2 sufficiently smooth functions and small parameter $0 < \epsilon \ll 1$. In this system x is the fast variable and y, z are the slow variables (since f, g_1, g_2 do not depend on ϵ, which is a small parameter, and hence $\dot{x}$ has to be much greater than $\dot{y}, \dot{z}$.

Let t denote the independent variable of 5.1, which is referred to as the *slow time scale*. By switching to the *fast time scale* $\tau = t/\epsilon$, one obtains the equivalent system:

$$\begin{aligned} x' &= f(x,y,z) \\ y' &= \epsilon g_1(x,y,z) \\ z' &= \epsilon g_2(x,y,z) \end{aligned} \tag{5.2}$$

where x' denotes the derivative of x with respect to τ and $\dot{x}$ the derivative of x with respect to t.

As $\epsilon \to 0$ the trajectories of 5.2 converge during fast epochs to solutions of the *fast subsystem* or *layer equations*:

$$\begin{aligned} x' &= f(x,y,z) \\ y' &= 0 \\ z' &= 0 \end{aligned} \tag{5.3}$$

[1] A complete explanation of this figure and its canards will be done in section 5.4.

implying that the fast flow is almost horizontal, following the principal direction of the fast variable x.

Conversely during slow epochs trajectories of 5.1 converge to solutions of the *slow subsystem* or *reduced problem*:

$$\begin{aligned} 0 &= f(x,y,z) \\ \dot{y} &= g_1(x,y,z) \\ \dot{z} &= g_2(x,y,z) \end{aligned} \tag{5.4}$$

which is a differential-algebraic equation.

One goal of GSPT is to use the fast and slow subsystems 5.3 and 5.4 to understand the dynamics of the full systems 5.2 and 5.1 for $\epsilon > 0$. First of all, the algebraic equation in 5.4 defines the so called *critical manifold*:

$$S := \{(x,y,z) : f(x,y,z) = 0\} \tag{5.5}$$

S can be called the *slow manifold* too, since the slow flow determined by 5.4 is constrained to lay on that manifold.

Assumption 1. S is supposed to be a smooth manifold.

Remark 1. The points of S are equilibrium points for the layer equations 5.3.

GSPT guarantees that normally hyperbolic invariant manifold (NHIM) S persists as locally invariant slow manifolds S_ϵ of the full problem 5.1 for sufficiently small ϵ. Moreover the restriction of the flow of 5.1 to S_ϵ is a small smooth perturbation of the flow of the reduced problem 5.4 [22].[2]

Normal hyperbolicity is often difficult to verify when there is only a single time scale. However, in our slow-fast setting, S consists entirely of equilibria (of the layer equations 5.3) and therefore the requirement of normal hyperbolicity of a compact subset $S_0 \subset S$ is satisfied as soon as all $p \in S_0$ are hyperbolic equilibria, i.e. if $f_x := \partial f/\partial x$ is uniformly bounded away from the imaginary axis for all $p \in S_0$. In that case the critical manifold S_0 is *normally hyperbolic*.[3]

Therefore GSPT breaks down at points on the critical manifold where normal hyperbolicity fails and we are interested precisely in the dynamics around those singularities. This can happen at points on S where their projection onto the space of slow variables is singular i.e. on the *fold lines* L, defined as the set of equilibria of 5.3 with a zero eigenvalue:

$$L := \{(x,y,z) \in S : f_x(x,y,z) = 0\}$$

The stability of points $p \in S$ as equilibria of the layer problem 5.3 depends on the sign of f_x: the fold lines divide the critical manifold S into attracting sheets S_a (where $f_x < 0$) and repelling sheets S_r (where $f_x > 0$).

Assumption 2. The critical manifold S is (locally) a folded surface, i.e.

$$S = S_a \cup L \cup S_r \tag{5.6}$$

In other terms we suppose $f_{xx} \neq 0$ for every point in the fold line L, obtaining:

$$L := \{(x,y,z) \in S : f_x(x,y,z) = 0, f_{xx}(x,y,z) \neq 0\} \tag{5.7}$$

This ensures that S actually has a fold and not a deflection tangent in L. A representation of this hypothesis fulfilled is shown in Figure 5.1.

[2] Fenichel Main Theorem, justifying these and other results, is shown in appendix A.
[3] See e.g. [24; 25] for more details.

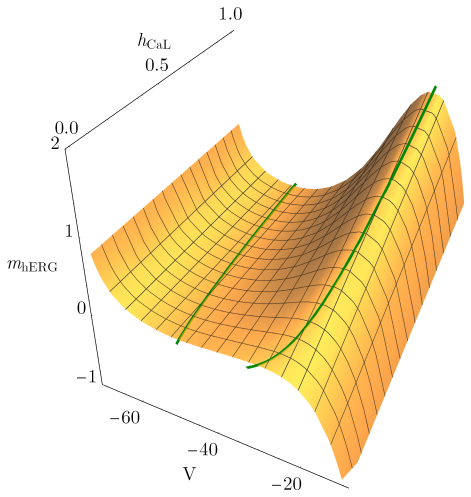

Figure 5.1: Folded surface with fold lines, obtained from the 3d-model with $g_{KV} = 0.15\ nS/pF$.

Without loss of generality, we assume that $f_z(p)|_{p\in L} \neq 0$ holds locally. It follows by the implicit function theorem that S is locally given as a graph $z = \phi(x, y)$. Hence the reduced problem 5.4 is projected onto the (x, y)-plane obtaining:

$$\left.\begin{aligned} -f_x\dot{x} &= f_y g_1 + f_z g_2 \\ \dot{y} &= g_1 \end{aligned}\right|_{z=\phi(x,y)} \tag{5.8}$$

where the first equation is obtained by deriving the algebraic equation $f = 0$ – that generates the folded surface – with respect to t. In fact this equation is no more necessary after imposing the equivalent constraint $z = \phi(x, y)$; conversely its derivative allow us to explicit the evolution of the fast variable onto the slow critical manifold S.

Finally, desingularization (i.e. rescaling time by $dt = -f_x dt'$) removes the singular term on the fold and gives the *desingularized system* of 5.9:

$$\left.\begin{aligned} \dot{x} &= f_y g_1 + f_z g_2 \\ \dot{y} &= -f_x g_1 \end{aligned}\right|_{z=\phi(x,y)} \tag{5.9}$$

Remark 2. The desingularized system 5.9 is equivalent to the original one 5.8 on the attracting sheets S_a but has opposite orientation on the repelling sheets S_r due to the time rescaling: for every point $p \in S_a$ by definition we have $f_x(p) < 0$, hence rescaling time by the factor $-f_x(p) > 0$ does not change the orientation; conversely on S_r $-f_x(p)$ is negative and then changes the direction of the flow. A graphical representation is shown in Figure 5.2.

5.2 Folded Singularities

Singularities of the desingularized system (i.e. points where $\dot{x} = \dot{y} = 0$) can be classed as ordinary or folded. Ordinary singularities are true equilibria onto S of the initial system 5.1 where g_1 is vanishing (and $g_2 = 0$ too – since we

supposed f_y and f_z to be nonvanishing on the vicinity of L). Folded singularities, on the other hand, are points along the fold lines L (hence where $f_x = 0$) where $f_y g_1 + f_z g_2|_{z=\phi(x,y)}$ vanishes.

Assumption 3. By resuming we supposed that the fold points $p \in L \subset S$ are generic in the sense of singularity theory, that is:

$$\begin{aligned} f(p) &= 0, \qquad & \frac{\partial f}{\partial x}(p) &= 0, \\ \frac{\partial^2 f}{\partial x^2}(p) &\neq 0, \qquad & D_{(y,z)} f(p) &\text{ has full rank} \end{aligned} \tag{5.10}$$

Definition 5.1. A fold point $p \in L$ satisfying:

$$f_y(p) g_1(p) + f_z(p) g_2(p) \neq 0 \tag{5.11}$$

is a *jump point* if there exists a trajectory of 5.8 starting at some point $q \in S_a$ and ending at p.

Jump points play a fundamental role in relaxation oscillations: under condition 5.11 the reduced system 5.8 becomes unbounded along the fold line L. Thus trajectories of system 5.1 reaching the vicinity of L subsequently jump away from the fold i.e. a fast transition away from the critical manifold S near L almost parallel to the x-axis occurs. This jumping behaviour near L is part of the mechanism leading to relaxation oscillations in system 5.1.

Thanks to GSPT, away from L there exist an attracting manifold $S_{a,\epsilon}$ and a repelling manifold $S_{r,\epsilon}$ with S_a and S_r as their singular limits. Moreover $S_{a,\epsilon}$ is locally invariant and the trajectories arrive in the vicinity of the fold line L after finite time. Then solutions are forced to jump away from the fold. If, after this fast transition from the fold, a global return mechanism projects the trajectory back onto the attracting manifold $S_{a,\epsilon}$ then periodic solutions are possibile and a relaxation oscillation appears, as it happens e.g. in Figure 5.4/d.

To obtain true MMOs including small amplitude oscillations the reduced flow on the (x, y)-plane 5.8 has to possess a folded singularity.

Definition 5.2. A fold point on $p_* \in L$ is also a *folded singularity* if 5.11 is violated in p_* i.e. if

$$f_y(p_*) g_1(p_*) + f_z(p_*) g_2(p_*) = 0 \tag{5.12}$$

Lemma 5.1. *It follows that folded singularities are equilibria of the desingularized system 5.9.*

Remark 3. Since the request is to satisfy an equation – rather than an inequality such as for jump points – folded singularities typically are isolated points.

As it is known from the theory of dynamical systems there are different types of equilibria p_* of the desingularized system 5.9. Let σ_1 and σ_2 denote the eigenvalues of the Jacobian of 5.9 evaluated at a folded singularity p_*, with $|\Re(\sigma_1)| > |\Re(\sigma_2)|$. We call p_* a:

$$\begin{cases} \text{folded saddle} & \text{if} \quad \sigma_1\sigma_2 < 0, \quad \sigma_{1,2} \in \mathbb{R}; \\ \text{folded node} & \text{if} \quad \sigma_1\sigma_2 > 0, \quad \sigma_{1,2} \in \mathbb{R}; \\ \text{folded focus} & \text{if} \quad \sigma_1\sigma_2 > 0, \quad \Im(\sigma_{1,2}) \neq 0. \end{cases}$$

The trajectories of the slow flow that lie along the eigendirections of the folded saddle or node connect the two sheets of the critical manifold through the folded singularity in finite time, even if it is slow. In these points the slow flow switches from incoming to outgoing. Such solutions are called *singular canards* and their persistence under small perturbations can give rise to complex dynamics. Of course, there are no canards for the case of a folded focus, since there is no real eigendirections.

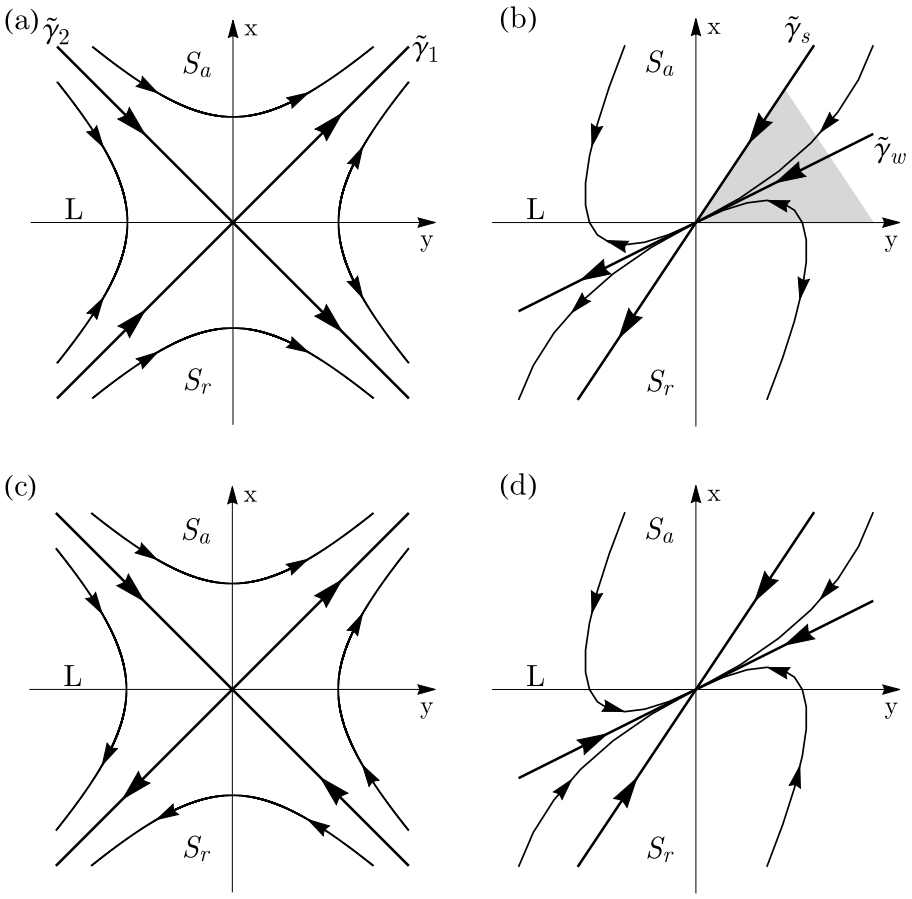

Figure 5.2: Phase portraits of the locally linearized slow flow near a folded saddle (a) and a folded node (b); the singular canards defined by the eigendirections are shown as thick lines. The corresponding desingularized slow flow is shown in panels (c) and (d), respectively. The darker shaded region of S_a is the funnel.

Remark 4. If we consider the sum and product of these eigenvalues $T := \sigma_1 + \sigma_2$ and $\Delta := \sigma_1 \sigma_2$ we can observe that the previous conditions are equivalent to:

$$\begin{cases} \text{folded saddle} & \text{if} \quad \Delta < 0; \\ \text{folded node} & \text{if} \quad 0 < \Delta < \frac{1}{4}T^2; \\ \text{folded focus} & \text{if} \quad \frac{1}{4}T^2 < \Delta. \end{cases}$$

Definition 5.3. For the case of the folded node the strong singular canard $\tilde{\gamma}_s$

and the fold curve F bound a full shaded sector of trajectories that cross from S_a to S_r by passing through the folded node. This sector is called the *funnel* of the folded node.

Concretely, the funnel is limited by the strong singular canard $\tilde{\gamma}_s$ and the fold line F, containing necessarily the weak singular canard. Similarly, the sector contained in the funnel between strong and weak singular canards will be the *sector of secondary canards.*

In the system we are going to study, most interesting folded singularities are folded nodes. And furthermore, in this case, if $T < 0$ then the negative eigenvalue is the greatest one and therefore trajectories of the slow flow 5.4 on S through p_* move from the attractive manifold S_a to the repelling one S_r. Hence we will talk about a *singular canard.* Conversely, when $T > 0$ these trajectories go from S_r to S_a, generating a so-called *faux canard* [8].

Let us deeply analyse canards in the next section.

5.3 Canards

We already know that *singular canards* are trajectories of the reduced flow 5.8 which pass at p_* from S_a to S_r. Moreover we know that they persist under perturbation of $\epsilon > 0$. In geometric terms, a canard corresponds to the intersection of the manifold $S_{a,\epsilon}$ and $S_{r,\epsilon}$ extended by the flow to the vicinity of the folded singularity; with this approach we will calculate them in chapter 7. Canards are not unique since the corresponding invariant manifolds $S_{a,\epsilon}$ and $S_{r,\epsilon}$ are not unique. By the way, for a fixed choice of the invariant manifolds we call their intersections *maximal canards.* In other words maximal canards can be seen as perturbations of singular canards which preserve the original behaviour.

Previously, we have also observed that *jump points* with a mechanism of global return allow the generation of relaxation oscillations; conversely *folded singularities* exhibit canards and small oscillations. In this section this type of singularities is studied in order to understand the canard generation.

The following theorem was taken from [9] and describes canards generation, depending on the type of folded singularity.

Theorem 5.2. *For the slow-fast system 5.1, with $\epsilon > 0$ sufficiently small, the following hold:*

1. *There are no maximal canards generated by a folded focus.*
2. *For a folded saddle the two singular canards $\tilde{\gamma}_{1,2}$ perturb to maximal canards $\gamma_{1,2}$.*
3. *For a folded node let $\mu := \sigma_s/\sigma_w > 1$. The singular canard $\tilde{\gamma}_s$ (the* strong canard*) always perturbs to a maximal canard γ_s.*
   - 3.1. *If $\mu \notin \mathbb{N}$, then the singular canard $\tilde{\gamma}_w$ (the* weak canard*) also perturbs to a maximal canard γ_w. We call γ_s and γ_w primary canards.*
   - 3.2. *For a folded node suppose $k > 0$ is an integer such that*

$$2k + 1 < \mu < 2k + 3 \quad \textit{and} \quad \mu \neq 2k + 2 \tag{5.13}$$

   i.e. $\mu \notin \mathbb{N}$. Then, in addition to $\gamma_{s,w}$, there are k other maximal canards, which we call secondary canards.

3.3. The primary weak canard of a folded node undergoes a transcritical bifurcation for odd $\mu \in \mathbb{N}$ and a pitchfork bifurcation for even $\mu \in \mathbb{N}$.

The proof of this theorem is based upon analysis of a canonical form of a slow-fast system near a folded singularity (such as 5.2). After a rescaling of coordinates (a *blow-up*), the canonical system becomes a regular perturbation problem and the variational equation along the *blown-up* singular canards becomes a classical Weber equation. Together with 5.10, properties of the Weber equation imply a transverse intersection of $S_{a,\epsilon}$ and $S_{r,\epsilon}$ for $\mu \in \mathbb{N}$ and, hence, existence of maximal canards (parts 2–3.1) for sufficiently small perturbations $0 < \epsilon < 1$. The proof of parts 3.2–3.3 is more involved and is based upon an extension of Melnikov theory [21] to show the bifurcation of secondary canards from the primary weak canard for $\mu - 1 \in \mathbb{N}$ [9].

Assumption 4. The reduced system 5.4 possesses a folded node singularity $p_* \in L$. Thus $\sigma_s \cdot \sigma_w > 0$ and in particular we assume it to be an attractive folded node i.e. $\sigma_s > 0,\ \sigma_w > 0$.

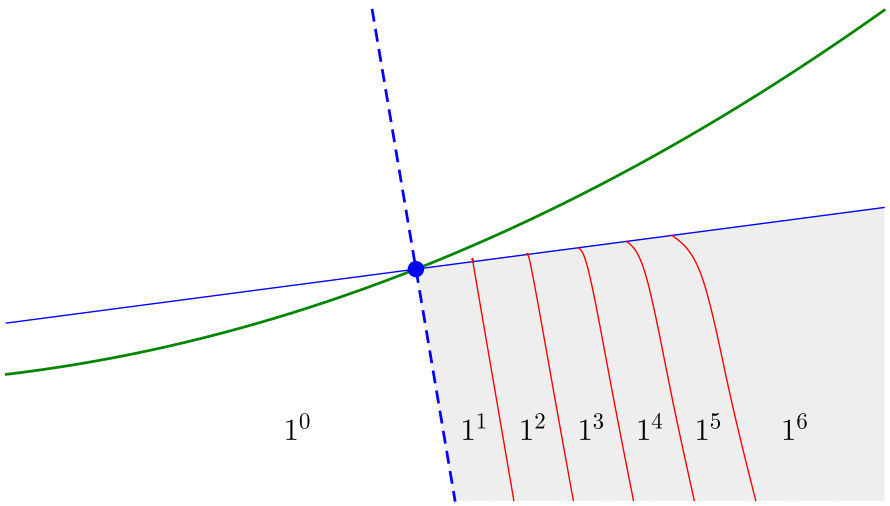

Figure 5.3: Secondary canards (red), primary strong canard (dashed bold blue), primary weak canard (thick blue), fold line (green), and sector of weak canards (light gray region). Secondary canards divide sector into subsectors which represent the domains of the MMO patterns $1^1 - 1^6$.

Remark 5. Simple algebraic calculations on 5.13 gives us the maximal number of secondary canard expressed like:

$$S_{max} = \left\lfloor \frac{\mu - 1}{2} \right\rfloor \tag{5.14}$$

where $\lfloor \cdot \rfloor$ denotes the floor function.

The case of the folded node is the more interesting for our study, since in chapter 7 we will find plenty of these singularities. We have already said in this

case many other intersections of the invariant manifolds occur and among them we find secondary canards too.

The presence of the secondary canard will divide their sector (shaded in Figure 5.3) into subsectors between primary maximal canards $\tilde{\gamma}_w$ and $\tilde{\gamma}_s$. Furthermore, trajectories within each subsector will be forced to take a certain number of turns around $\tilde{\gamma}_w$ when passing through p_* resulting in SAOa [17].

The widths of the rotational sectors in Figure 5.3 are very similar, and depend on ϵ. In fact all sectors are very small, except for the sector corresponding to maximal rotation, which is bounded by the last secondary canard and the primary weak canard.

The entry point of the trajecory in the sector of secondary canards influences the amplitude of the SAOs too, and not only their number.Thus, if a trajectory enters in close to a maximal canard the amplitude of the SAOs will be larger than if the trajectory entered in between between two maximal canards [26].

5.4 Example: Van der Pol Equation

We are interested in applying GSPT to 3d-systems; still, in order to better understand what we are going to do, we decided to follow the approach in [27] and show a basic 2-dimensional example, applied to the Van der Pol equation, where canard phenomenon was firstly seen. These canards will be generated by the appearance of a Hopf bifurcation instead of that of a folded node, still it will be useful in order to start visualizing these mathematical objects.

As we already said in the introduction to this chapter, in 2d-system maximal canards occur for discrete values of the control parameter, unlike in 3d maximal where they are persistent under small parameter changes. This means that it is complicated to "see" a canard in those systems: the parameter λ was fixed near the well precised value 0.99349093 in order to show the canards[4], which is a value ϵ-distant from the fold happening at $\lambda = 1$. Anyway, this example would like to help the comprehension of what we have just explained, allowing a more immediate 2d-visualization.

Let us consider the system of equations:

$$\begin{aligned} \epsilon \dot{x} &= f(x, y) \coloneqq y - \frac{x^3}{3} + x \\ \dot{y} &= \lambda - x \end{aligned} \tag{5.15}$$

where $0 < \epsilon \ll 1$ and λ are parameters.

Rewriting 5.15 in terms of the slow time $\tau = \epsilon t$, one finds that the corresponding "slow nullcline" is given by $x = \lambda$. As λ passes through 1, this slow nullcline moves through the lower fold point of S, which triggers the onset of the canard explosion, see Figure 5.4. Finally, for $\lambda > 0$ sufficiently "large", the dynamics of 5.15 enters the relaxation regime [27]. Let us proceed with some calculations, helping us to understand this figure and its relationship with the previously explained Geometric Singular Perturbation Theory (GSPT).

We can easily calcute the equilibrium of the reduced problem, obtained from

[4] See Figure 5.4.

5.15 for $\epsilon = 0$:

$$\begin{aligned} 0 &= f(x,y) \\ \dot{y} &= \lambda - x \end{aligned} \tag{5.16}$$

and find that the only equilibrium is the point $\left(\lambda, \frac{\lambda^3}{3} - \lambda\right)$.

The "fast nullcline" S for 5.15 is given by $f(x,y) = 0$. It is a S-shaped curve and, moreover, a curve of equilibria for the *layer problem*:

$$\begin{aligned} x' &= f(x,y) \\ y' &= 0 \end{aligned} \tag{5.17}$$

obtained by putting $\epsilon = 0$ in the slow system. S is normally hyperbolic away from the local minimum and maximum $p_\pm = \left(\pm 1, \mp\frac{2}{3}\right)$ of the cubic, where S has a fold with respect to the fast variable x. At $p_\pm$ normal hyperbolicity fails, since:

$$f_x(p_\pm) = 1 - x^2\big|_{p_\pm} = 0$$

Hence $p_\pm$ are the fold points and naturally decompose the critical manifold S into three branches: the dynamics will be unstable between them (where $f_x > 0$) and stable out of them (where $f_x < 0$), as we can see in Figure 5.4/a.

Far from S the dynamics is entirely controlled by the direction of the fast variable x, estimating that the flow of the original system 5.15 will be almost parallel to that direction.

On the other side, near the folded curve S we have to derive the equation $f = 0$ and consider the projection of the reduced problem 5.16 onto the folded curve:

$$\left.\begin{aligned} -(1-x^2)\dot{x} &= \dot{y} \\ \dot{y} &= \lambda - x \end{aligned}\right|_S$$

Thus, we obtain the equation that describes the dynamics of the system on the slow curve:

$$\dot{x} = \left.\frac{\lambda - x}{x^2 - 1}\right|_S \tag{5.18}$$

The direction of the slow flow on S is indicated in Figure 5.4 by blue and red arrows. The slow flow does depend on λ, because the direction of the slow flow is partly determined by the location of the equilibrium at $x = \lambda$ on S.

When $x = \pm 1$ and $\lambda \neq x$ the equation 5.18 is singular. Thus we can write the desingularized reduced flow by rescaling the time with the factor $x^2 - 1$, which gives us:

$$\dot{x} = \lambda - x\big|_S \tag{5.19}$$

As we already remarked and showed in Figure 5.2, this time rescaling reverses the direction of time on the repelling branch S_r.

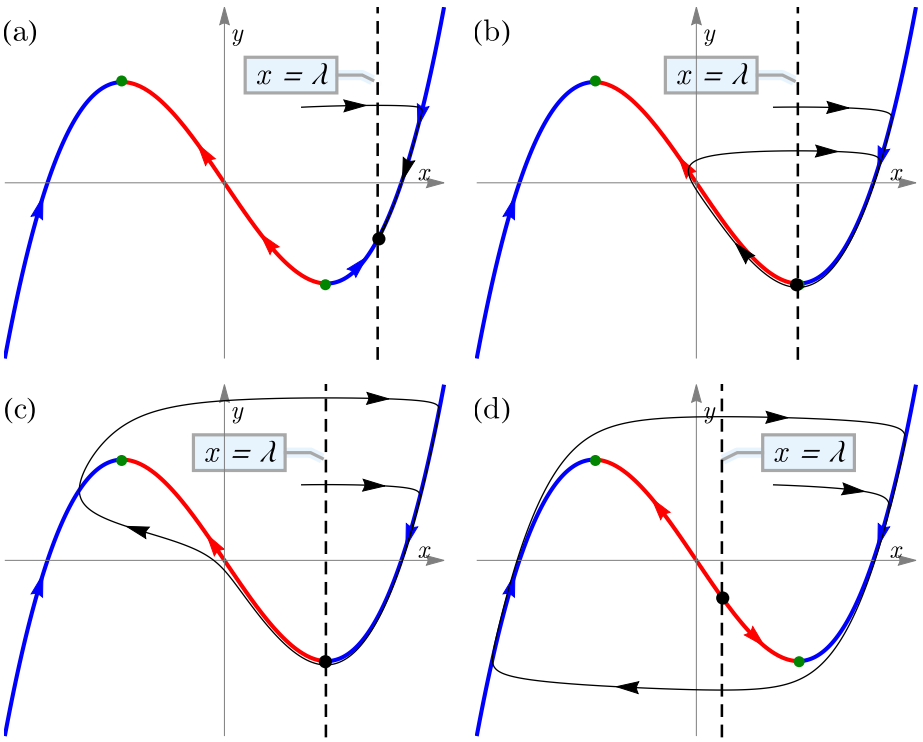

Figure 5.4: Nullcline (dashed line) movement leading to a canard explosion: as it passes through $x = 1$, one observes a transition from a stable equilibrium (a) with $\lambda = 1.5$ via a family of solutions ((b) "headless canard", with $\lambda = 0.9934909315$, (c) "canard with head", with $\lambda = 0.99349093$) to a full-scale relaxation oscillation (d) $\lambda = 0.25$. Every simulation was obtained with $\epsilon = 0.05$ and with initial value $x(0) = 0.75$, $y(0) = 0.5$. The S-shaped nullcline is plotted in blue (where it is stable) and red (where it is unstable), the equilibrium is the big black dot at the intersection of the nullclines and finally fold points $p^{\pm}$ are the little green dots.

Let us focus on relaxation oscillations: in Figure 5.4/d we can observe that the equilibrium is a source and that temporal evolution leads to a stable periodic orbit Γ_ϵ (the black oriented curve). This orbit is composed of two fast trajectories starting near the fold points $p_\pm$ concatenated with segments of S: it follows the slow flow on S until it reaches a fold point and then it *jumps*, that is, it makes a transition to a fast trajectory segment that flows to the other branch of S. The same mechanism also returns Γ_ϵ to the initial branch of S [9].

Furthermore, if we ask that $\epsilon = 0$ a singular orbit Γ would appear, with fast trajectories completely horizontal starting exactly from the fold points. Krupa and Szmolyan showed that the cycle Γ_ϵ is strongly attrancting and that it approaches to Γ in the Hausdorff distance as $\epsilon \to 0$ [16]. And moreover, Desroches et al. claims that Γ_ϵ lies $O\left(\epsilon^{3/2}\right)$ close to Γ.

Finally, let us focus on Hopf bifurcation and canard explosion. The unique equilibrium of the Van der Pol system 5.15 is a source for $|\lambda| < 1$ and a sink for $|\lambda| > 1$; a Hopf bifurcation occurs in $\lambda = \pm 1$. This means that, in this equilibrium, the dynamical system has two purely imaginary eigenvalues cross-

ing the imaginary axis with nonzero speed as λ is varied. As a result, a family of periodic orbits arises from the bifurcation point. The Hopf bifurcation is called *supercritical* if those periodic orbits are stable, *subcritical* if they are unstable. As we saw in Figure 5.4/d a family of stable periodic orbits exists in the parameter interval $|\lambda| < 1$, therefore those Hopf bifurcations are supercritical.

The Hopf bifurcation at $\lambda = 1$ occurs when the equilibrium moves over the fold point p_+: it is simple to verify that the eigenvalues of 5.15 at the Hopf bifurcation have magnitude $O\left(\epsilon^{-1/2}\right)$, so that the periodic orbit is born with an intermediate period between the fast $O(\epsilon)$ and the slow $O(1)$. The amplitude of these periodic orbits grows rapidly (as we can see comparing Figure 5.4/b-c) and it is called *canard explosion*.

5.5 Last Considerations

In our model we will face folded node type canard generated MMOs. Then it is important to remember that the previous example referred to a singular Hopf generated MMOs. The distinction between these two phenomena comes mainly from the following fact: in the former case there is no equilibrium point of the original system in the neighborhood where the small (subthreshold) oscillations occur, while in the latter there is (we have just seen the equilibrium moving through the point p^+ and generating a canard in the previous example).

In fact, the folded node is an equilibrium of the desingularized flow on the critical manifold but *not* an equilibrium of the original fast-slow system. It belongs to the fold and a whole family of solutions crosses through it from the attracting to the repelling branch of the slow manifold [28]. Resuming what we stated in this chapter, the folded node possesses a unique (strong) canard and non-unique (weak / secondary) canards. The strong canard and the fold line delineate a trapping region, called funnel. Then any solution that ends up in the funnel passes near the folded node and is forced to enter the repelling sheet.

In the singular Hopf case, an equilibrium of the original fast-slow system exists in the neighborhood of the curve of folds. In fact, a Hopf bifurcation point is on the critical manifold but displaced from the fold by $O(\epsilon)$-distance (that is why in the previous example we found the canard in the vicinity of the fold but not precisely on it).

Chapter 6

Reduction to a 4d-Model

If we want to apply the theory exposed in chapter 5 we have to reduce the initial 8d-model to a 3-dimensional system. Then, we have to find a clever method to pass from eight to three variables without losing too much informations.

6.1 Resume of the Method

After having analised the real parts of the eight eigenvalues related to the jacobian matrix of the 8d-system we will remark that four of them are nearly always negligible, implying that their variables do not influence strikingly the dynamics of the system.

Then we will be authorised to rewrite four of the system variables as function of membrane potential V. Choosing which variables will still be independent and which ones will be rewritten is not trivial, but I followed suggestions from Izhikevich found in [29].

Previous reduction schemes for the Hodgkin-Huxley system[1]:

$$\begin{aligned} C\dot{V} &= I - g_K n^4 (V - E_K) - g_{Na} m^3 h (V - E_{Na}) - g_L (V - E_L) \\ \dot{n} &= (n_\infty(V) - n)/\tau_n(V) \\ \dot{m} &= (m_\infty(V) - m)/\tau_m(V) \\ \dot{h} &= (h_\infty(V) - h)/\tau_h(V) \end{aligned} \tag{6.1}$$

have exploited the rapidity of sodium current activation to eliminate the sodium activation as a dynamic variable. In fact computer simulations by Krinsky and Kokoz [30] have shown that there is a relationship between the sodium inactivation h and the potassium activation n, namely:

$$n(t) + h(t) \approx 0.84$$

Then, plotting on the (n, h) plane reveals that the orbit is near the straight line:

$$h = 0.89 - 1.1n$$

We can use this relationship in the voltage equation to reduce 6.1 to a three-dimensional system.

[1] The entire construction of this model an be found in [11]

The similar time scales of the sodium inactivation h and potassium activation n have been used to combine h and n into a single *recovery* variable. Hence this method will be useful for variables linked by similar time scales.

A similar approximation can be applied to really slow variables, such as m_{hERG} and h_{hERG}, which can be seen pretty much like constants or slightly steep linear functions.

For the fastest variables another approximation seems to be more reasonable: since they are so fast we could suppose that their gates activate almost instantaneously. From a mathematical point of view, this implies that these variables could be near to their steady-state functions.

6.2 Eigenvalue Analysis of the 8d-Model

Let us come back to our 8d-model constructed in chapter 2 and consider the jacobian matrix associated to the model in a generic point of the domain D.[2] The jacobian was calculated analitically using Mathematica and different behaviours seen in chapter 4 were reproduced choosing the values stated before for g_{KV}.

In the stable case, with $g_{KV} = 0.05\ nS/pF$ the eigenvalues real part can be seen in the barplot in Figure 6.1.

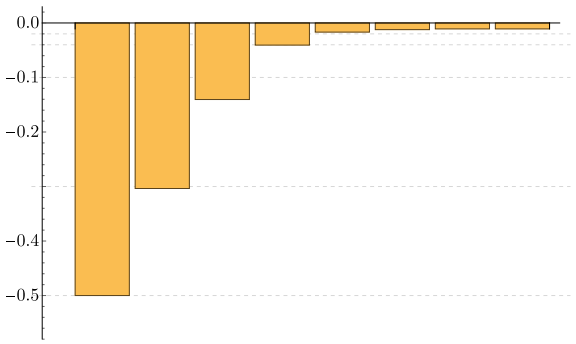

Figure 6.1: Barplot of the eight eigenvalues real part with $g_{KV} = 0.05\ nS/pF$ and default values of parameters indicated in Table 2.1.

It can be noticed that the absolute value of the real parts of four eigenvalues are smaller than 0.02 and another is about to 0.04. Of course, all of them are negative, which is obvious for a stable equilibrium.

During spiking and bursting the eigenvalues change as a function of time and therefore we have to compute a more complex analysis: for both of these cases we will plot three different graphs. In the first one it will be shown the curve of the potential evolving towards time. In the second graph we will visualize the real part of the eight eigenvalues all along the evolution of the system.[3]. The last graph will be a bar chart were we will plot those eigenvalues in some "more interesting" points; those points were chosen, looking to both the previous images, at specific instants in order to represent at best the possible configurations of the cell: when it is depolarizing or repolarizing, when potential

[2] We can suppose $D = (-80, 10) \times (0, 1)^7$ since the membrane potential bounded to that clamp in simulations and the other seven variables are bounded between 0 and 1 by construction.

[3] From this point until the end of the chapter I will write simply "eigenvalue" to indicate the "real part of the eigenvalue" in order to speed up the reading and help the comprehension.

is almost-constant near to the rest state, or when it is oscillating on the plateau generated from the bursting behaviour.

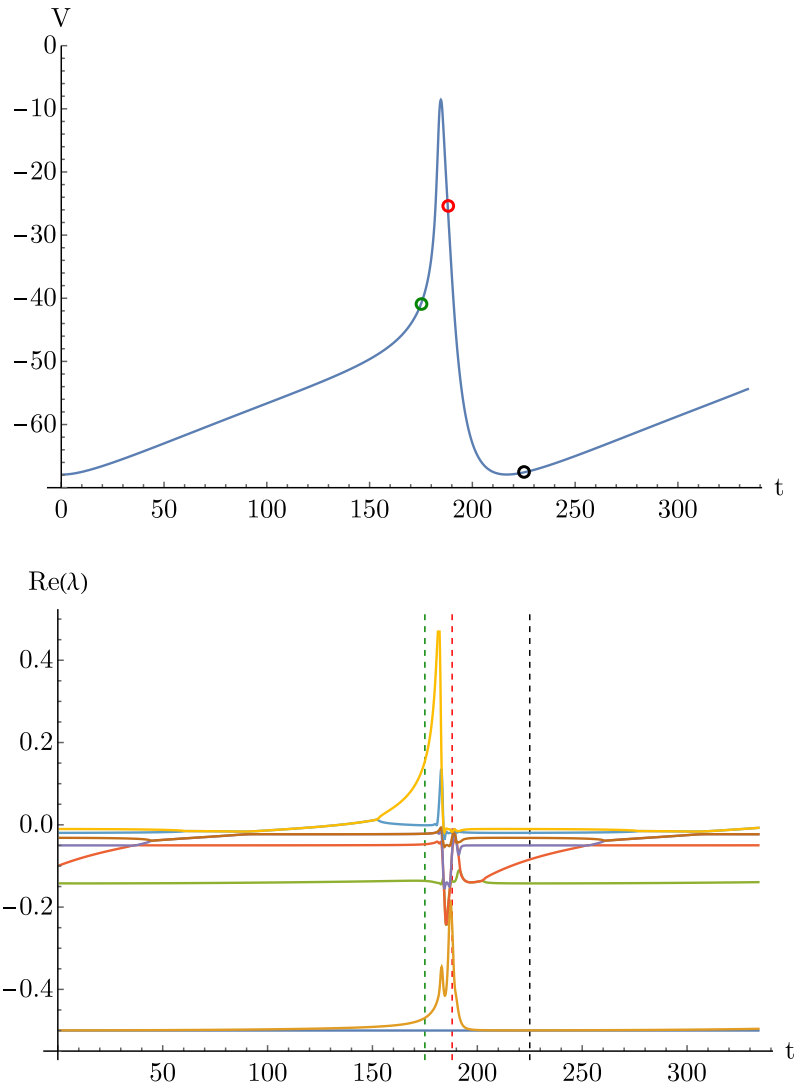

Figure 6.2: Up: plot of V. Down: eigenvalues real part variation. Default values of parameters indicated in Table 2.1. Coloured circles and corresponding dashed lines denote the points at which the eigenvalues will be plotted in Figure 6.3.

In the spiking case we consider default $g_{KV} = 1\ nS/pF$ and study the eigenvalues along the evolution of the system, which can be seen in Figure 6.2/down. Three instants where chosen to plot in Figure 6.3 the eigenvalues at different potentials V, plotted in Figure 6.2/up in a bar chart.

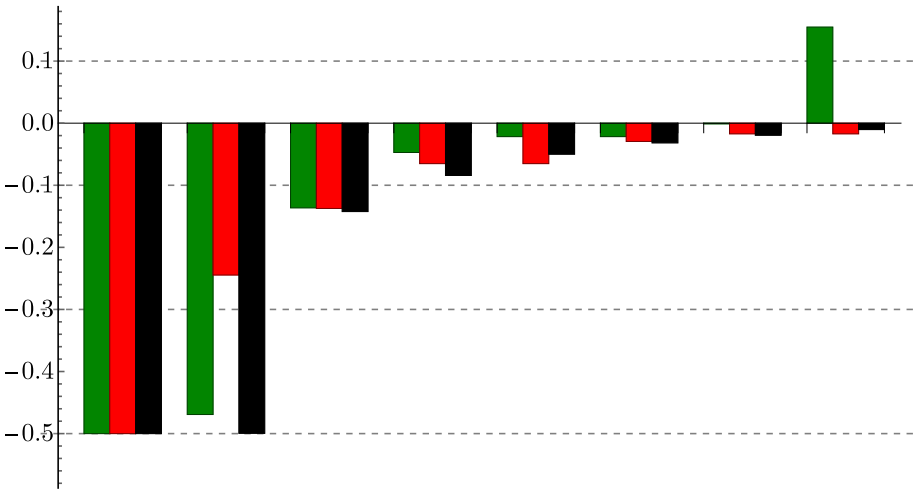

Figure 6.3: Barplot of the eight eigenvalues real part with default values of parameters indicated in Table 2.1.

When the cell is totally depolarized (black colour in the previous figures) or is repolarizing (red colour) five eigenvalues are smaller than 0.1, but during the depolarization (highlighted in green), and in particular near to spiking phase, one of them becomes positive, causing a destabilisation of the system, and its absolute value can overstep 0.4. Then we can suppose that this dimension cannot be eliminated very easily.

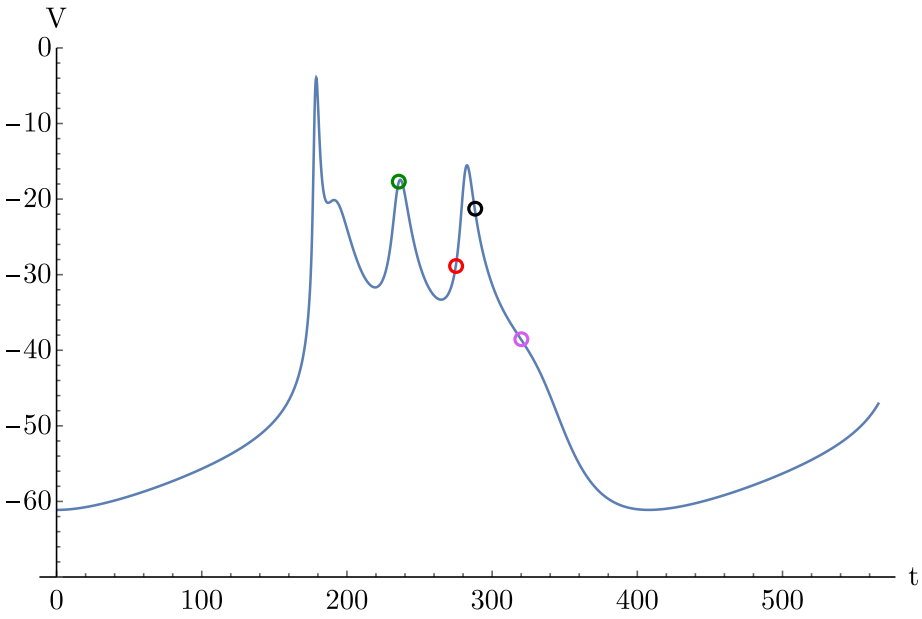

Figure 6.4: Plot of V with $g_{KV} = 0.2\ nS/pF$ and default values of parameters indicated in Table 2.1. Coloured circles denote the points were the eigenvalues will be plotted in Figure 6.3.

Finally, in order to study the bursting case, we consider $g_{KV} = 0.2\ nS/pF$ and look for the eigenvalues along the evolution of the system, which can be seen in Figure 6.5. Three instants where chosen to plot in Figure 6.6 the real part of the eigenvalues at different potentials V, plotted in Figure 6.4 in a barplot.

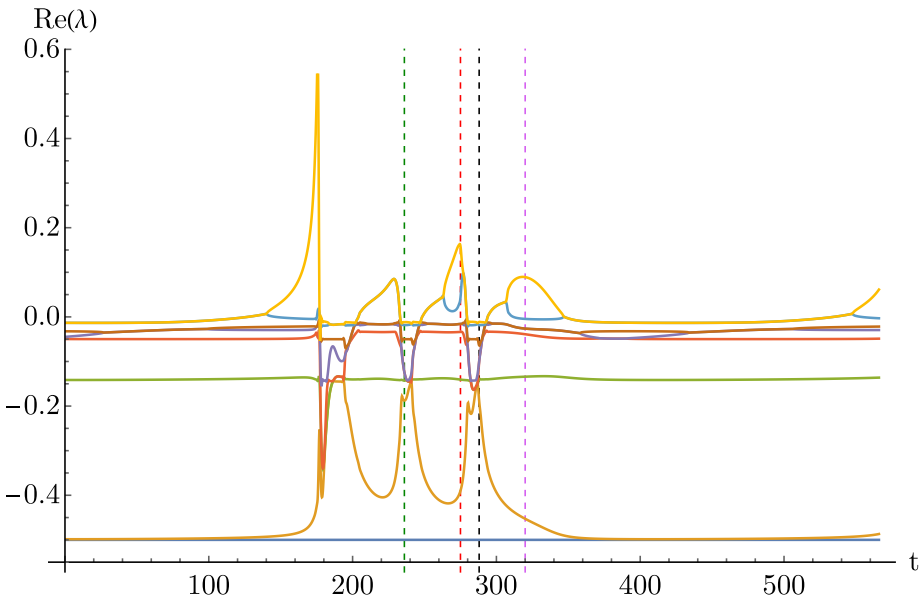

Figure 6.5: Eigenvalues real part variation along the evolution of the bursting system ($g_{KV} = 0.2\ nS/pF$). Dashed lines indicate the time position corresponding to the circles of the same colours in the previous figure at which the eigenvalues will be plotted in Figure 6.6.

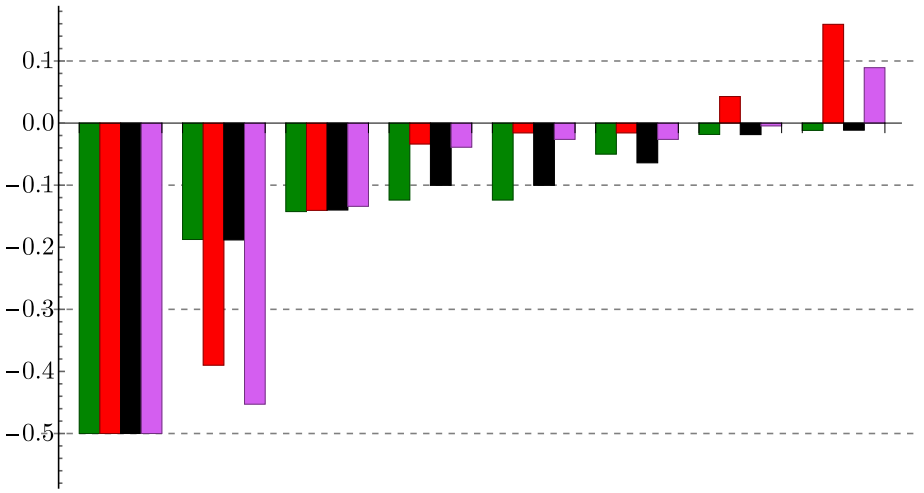

Figure 6.6: Barplot of the eight eigenvalues real part with default values of parameters indicated in Table 2.1.

Looking to Figure 6.5 we can remark that eigenvalues become positive many times during bursting activity, being constrained to the plateau interval and repolarization phase at most: e.g. at the purple instant the system presents one positive eigenvalue. This phenomenum obviously causes instability during long periods, even though the system carries on oscillating from stable to unstable configuration (e.g. green and black instants present stability during and after plateau little spikes, red instants presents two positive eigenvalues, therefore instability).

During depolarization and repolarization the behaviour is similar to the one we observed in simple spiking activity so it has not been shown in the barplot.

Looking to all the previous figures of this chapter we can remark something more about the 8d-model. First of all, one eigenvalue – the light green one – is seen to be stable to the constant value of -0.5 in all types of activities; the third one is almost constant too, being kept between -0.15 and -0.13. When the membrane potential is in a constant or almost-constant condition all the eigenvalues keep negative; conversely when depolarization becomes too steep, then just before spiking activity, an eigenvalue change of sign and explodes around $0.4 - 0.5$. It can oscillates from one to the other sign during bursting and another eigenvalue can change of sign too, even if this will not modify too much the dynamics since the system was unstable yet.

Hence, we decided to neglect four of them, which seems very reasonnable looking to spiking activities and a little more risky, but still acceptable, for the bursting case (since during and after plateau-spikes the forth and fifth eigenvalues do not seem to be that negligible).

Now we know how many variables we should be able to eliminate; anyway we still do not know which of them should be changed: the next section will help us taking this decision.

6.3 Variables Reduction

As I stated before we should considerate the variables speed in order to decide how to approximate them.

Velocity	T.D.F.	Value $[ms]$
Fast	τ_{hCaT}	7
	τ_{hNa}	2
	τ_{mBK}	2
Medium	$\tau_{mKV}(V)$	$(2, 32)$
	τ_{hCaL}	20
Slow	τ_{hhERG}	50
	τ_{mhERG}	100

Table 6.1: Variables speed with default time delay factors (T.D.F.) from Table 2.1. $\tau_{mKV}(V)$ depends on V as we stated in chapter 2 (boundaries for this variable can be found in appendix C).

In chapter 3 we stated that the speed of the variable

$$x \in \{h_{CaT}, h_{CaL}, h_{Na}, m_{BK}, m_{KV}, m_{hERG}, h_{hERG}\}$$

depends linearly on its time delay constant τ_x. Hence Table 6.1 allows us to divide those variables in three cathegories. Remark that the fast variable V is excluded from this analysis since all the other variables depend on it.

As supposed in the first section of this chapter let us try to approximate fast variables with their steady-state functions. Simulations of each fast variable depending with respect to V and their steady-state functions are shown in Figure 6.7.

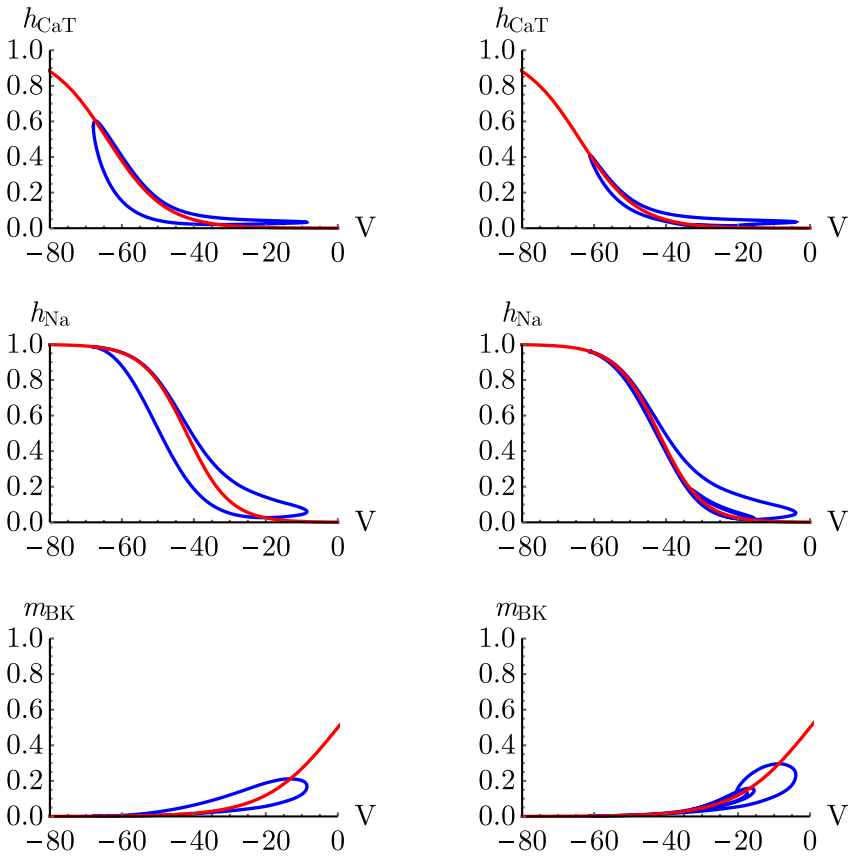

Figure 6.7: Fast time scaled variables simulations (blue) with their steady-state functions (red).

Previous considerations lead us to this choice and plots in Figure 6.7 seem to confirm our suppositions. Anyway I bring a further study in appendix D: a numerical non-linear interpolation was performed for both spiking and bursting simulations using Boltzmann functions; the standard error could be considered quite small and parameters found were really close to the steady-state function ones. Both, standard error with respect to the data and distance between the parameters, were seen to reduce in the bursting activity with respect to the spiking.

Thanks to Figure 6.8 we can also remark that medium-fast variables $\{h_{CaL}, m_{KV}\}$ seems not to be sufficiently near to their steady-state functions.

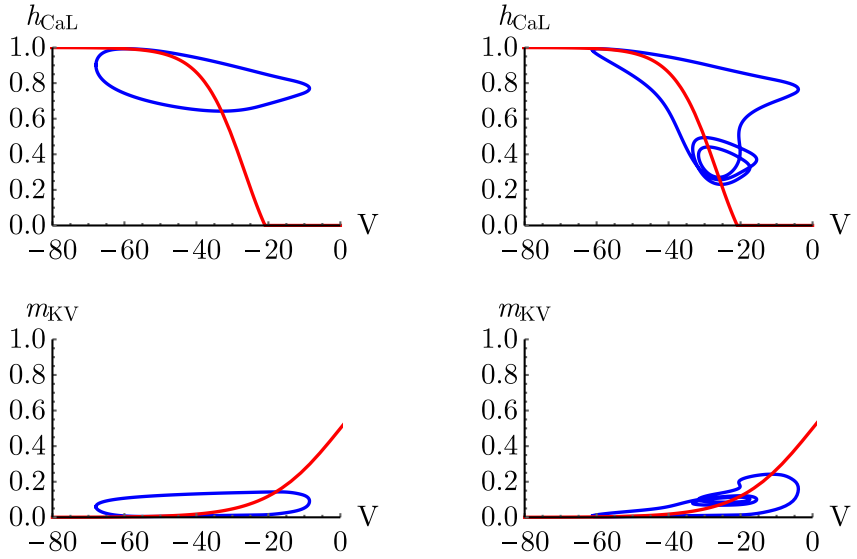

Figure 6.8: Medium time scaled variables simulations (blue) with their steady-state functions (red).

Finally, let us consider slow variables $\{h_{hERG}, m_{hERG}\}$. As stated before, since they are much more slow than the other it seems reasonable to approximate them with a constant:

$$m_{hERG} = 0.15$$
$$h_{hERG} = 0.58$$

By the way, looking to Figure 6.9 I chose not to interpolate simulations this time: hence we simulated spiking and bursting activity for one period respectively every millisecond. We can easily remark that their are not uniformely distributed at all and therefore consider to try a better approximation.

Thanks to a linear fitting of the bursting data I obtained the line:[4]

$$h_{hERG}(V) = -0.007V + 0.22 \tag{6.2}$$

Figure 6.9 illustrates possible approximations and their steady-state functions too: as it was expected they are really badly approximated by these functions since they are too slow to be considered to activate instantaneously.

Anyway our final aim is to perform a fast-slow analysis, hence we should preserve the fast-slow dynamics of the model: in order to do that one slow variable must be kept. The slowest one will allow a major time scale skip and therefore I chose to approximate h_{hERG} as proposed in Equation 6.2.

[4] I chose to keep the fitting made on bursting - instead of spiking - activity since as we saw before in bursting even non-linear approximations worked better. We could interpretate this fact by considering that during bursting much more information is conserved for two reasons: the period is longer than during spiking and bursting contains both the stable (plateau) and the spiking behaviour.

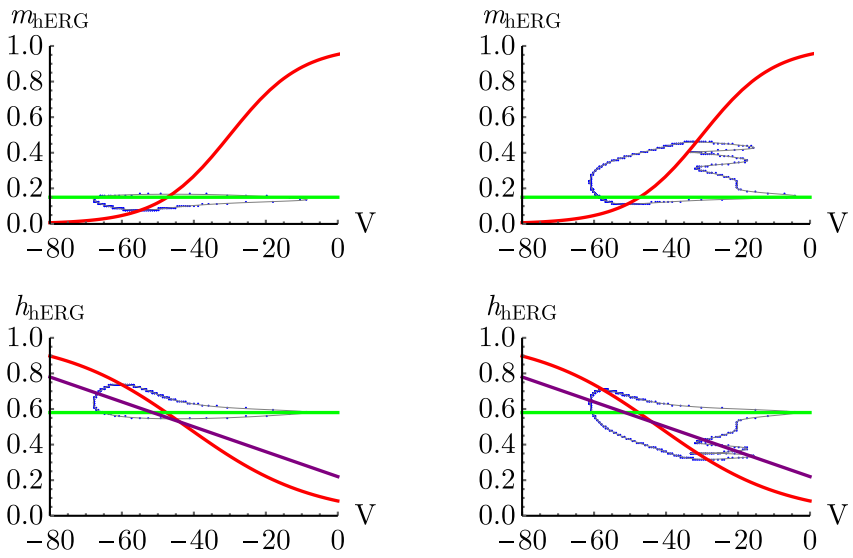

Figure 6.9: In this figure slow time scaled variables simulations were evaluatesd (blue dots interpolate with gray curves). We can also see their steady-state functions (red) and constant values intended to approximate them (green). For h_{hERG} the interpolating linear function for the bursting case has been plotted too (purple).

6.4 4d-Model

Hence in this chapter the initial 8d-system has been reduced to only four variables:

$$V,\, h_{CaL},\, m_{KV},\, m_{hERG}$$

We have obtained the new system of the form:

$$\begin{aligned}
\frac{\mathrm{d}V}{\mathrm{d}t} &= -I_{Total}\left(V, h_{CaL}, m_{KV}, m_{hERG}\right) \\
\frac{\mathrm{d}h_{CaL}}{\mathrm{d}t} &= \frac{h_{CaL,\infty}(V) - h_{CaL}}{\tau_{hCaL}} \\
\frac{\mathrm{d}m_{KV}}{\mathrm{d}t} &= \frac{m_{K_V,\infty}(V) - m_{K_V}}{\tau_{mKV}(V)} \\
\frac{\mathrm{d}m_{hERG}}{\mathrm{d}t} &= \frac{m_{hERG,\infty}(V) - m_{hERG}}{\tau_{mhERG}}
\end{aligned} \tag{6.3}$$

One more variable has to be reduced in the following, in order to apply GSPT. Before doing that, let us briefly verify that the three different behaviours we are interested of have been preserved during this first reduction of the model and that these behaviours still depends on g_{KV}.

In the following figures we can see all those behaviiours. In particular we obtain the:

- stable system for $g_{KV} = 1.8\ nS/pF$ (Figure 6.10)

- spiking activity for $g_{KV} = 1\ nS/pF$ (Figure 6.11)
- bursting activity for $g_{KV} = 0.05\ nS/pF$ (Figure 6.12)

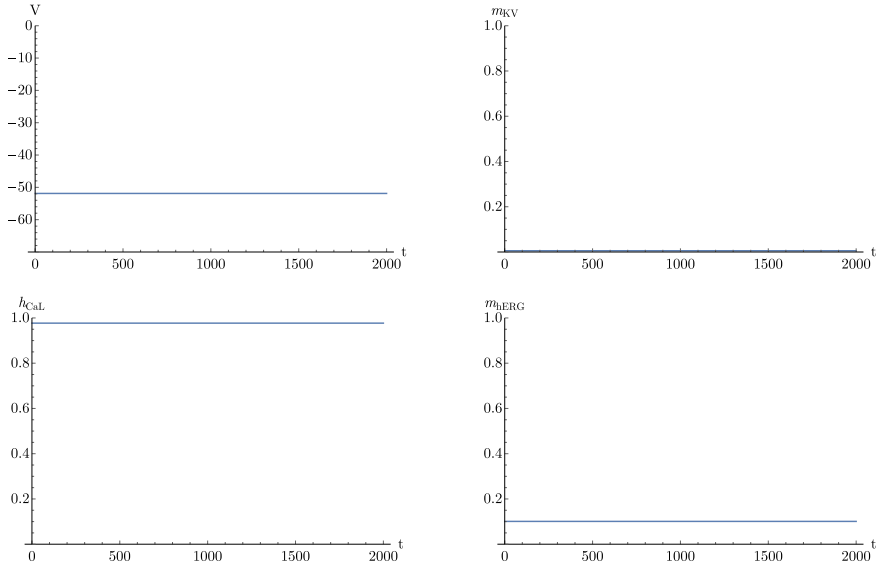

Figure 6.10: Example of stable case for the 4d-model obtained with $g_{KV} = 1.8\ nS/pF$

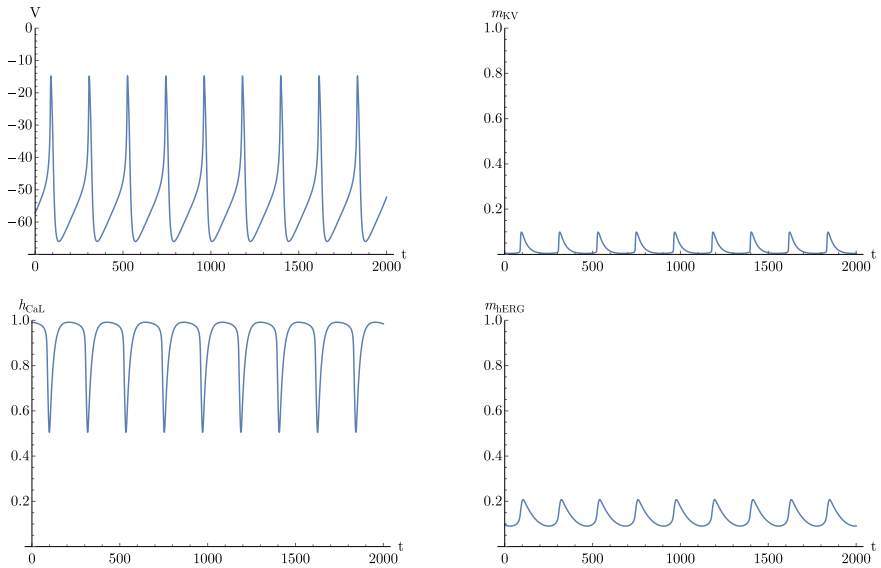

Figure 6.11: Example of spiking activity for the 4d-model obtained with $g_{KV} = 1\ nS/pF$

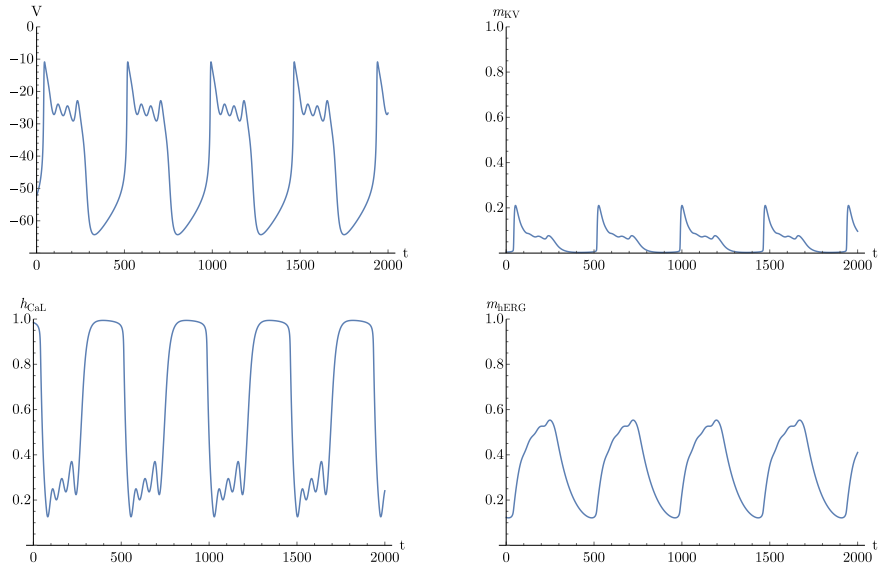

Figure 6.12: Example of bursting activity for the 4d-model obtained with $g_{KV} = 0.05\ nS/pF$

Chapter 7

3d-Model

In this chapter I would like to obtain a 3-dimensional system by reducing one dimension of the 4d-model, that we have already constructed, in order to implement GSPT exposed in chapter 5. We will observe that stable, spiking and bursting behaviour will still be present in the dynamics of the new system, justifying therefore its construction. Finally we will focus on the bursting activity and show that it is due to canard-generated Mixed Mode Oscillations.

7.1 Choice of the Model

In chapter 6 we have already noticed that the four variable of the system 6.3 can be splitted in:

- one fast variable V
- two medium variables h_{CaL}, m_{KV}
- one slow variable m_{hERG}

We can remark that two variables have the same speed. Therefore, remembering the approach found in [29] and exposed in chapter 6 we can try to plot m_{KV} with respect to h_{CaL} and to fit the data with a linear function.

As seen in Figure 7.1 linear interpolation gives us the function:

$$m_{KV}(h_{CaL}) = -0.12h_{CaL} + 0.13 \tag{7.1}$$

Thanks to the explicitation of m_{KV}, there are no more risks of misunderstanding the variables name; therefore, starting from now and until the end of this chapter, I will use h and m in place of h_{CaL} and m_{hERG}.

We finally obtain the three-dimensional system:

$$\begin{aligned} \frac{\mathrm{d}V}{\mathrm{d}t} &= -I_{Total}\,(V,h,m) \\ \frac{\mathrm{d}h}{\mathrm{d}t} &= \frac{h_\infty(V)-h}{\tau_h} \\ \frac{\mathrm{d}m}{\mathrm{d}t} &= \frac{m_\infty(V)-m}{\tau_m} \end{aligned} \tag{7.2}$$

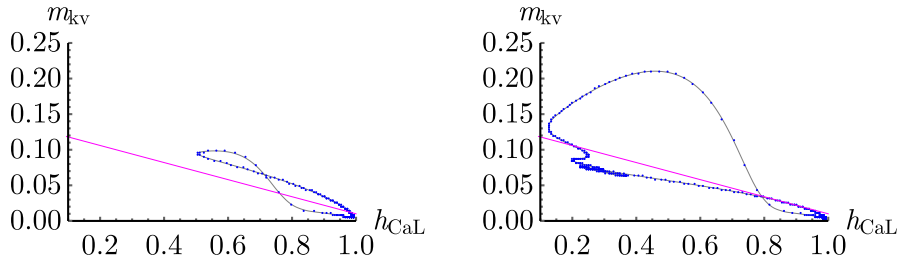

Figure 7.1: Magenta line is the linear interpolation of spiking ($g_{KV} = 0.05\ nS/pF$) and bursting ($g_{KV} = 1\ nS/pF$) data. On the left side the plot show also the spiking simulation, on the right side the bursting one.

Simulations are plotted in Figure 7.2, showing that the three types of dynamics are still preserved in this model.

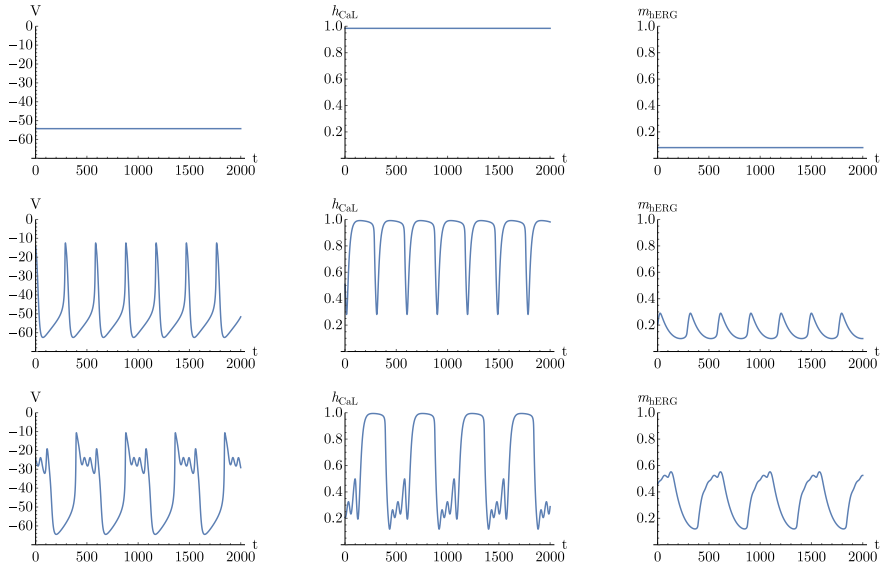

Figure 7.2: Simulations for the 3d-model with default parameters and modifying g_{KV}: stable behaviour for $g_{KV} = 1\ nS/pF$ (first row), spiking activity for $g_{KV} = 0.5\ nS/pF$ (second row) and bursting activity for $g_{KV} = 0.05\ nS/pF$ (third row).

7.2 Structure of the 3d-Model

If we follow the notation of chapter 3 and remember the definitions 3.4 we have:

$$\epsilon \leq 0.025, \qquad \delta_h = 0.2, \qquad \delta_m = 1 \tag{7.3}$$

Then we can claim that V is the fastest variable and rewrite the system in

the form studied in chapter 5:

$$\begin{aligned}\epsilon\frac{\mathrm{d}V}{\mathrm{d}t} &= -I_{Total}\left(V,h,m\right)\\ \frac{\mathrm{d}h}{\mathrm{d}t} &= \frac{h_\infty(V)-h}{\tau_h}\\ \frac{\mathrm{d}m}{\mathrm{d}t} &= \frac{m_\infty(V)-m}{\tau_m}\end{aligned} \tag{7.4}$$

This let us apply GSPT to our 3d-model. I decided to use default parameters of Table 2.1 with $g_{KV} = 0.05\ nS/pF$, for the moment.

In order to simplify and obtain a system with the same notation of 5.1, we define:

$$\begin{aligned}f\left(V,h,m\right) &:= -I_{Total}\left(V,h,m\right)\\ g_1\left(V,h\right) &:= \frac{h_\infty(V)-h}{\tau_h}\\ g_2\left(V,m\right) &:= \frac{m_\infty(V)-m}{\tau_m}\end{aligned} \tag{7.5}$$

We have to remark that g_2 (respectively g_1) does not depend on h (resp. m) and that the dependence on m (resp. h) is linear. By expliciting f we can also observe that it is linear with respect to both, h and m. Hence, when we ask that $f = 0$ in order to calculate the folded surface S defined in Equation 5.5 we can easily explicit m with respect to V and h: this leads us to the expression $m = \phi\left(V,h\right)\ \forall\left(V,h,m\right) \in S$. Fold lines are obtained by asking $f_V = 0$ too and it gives us a similar condition where $h = \psi\left(V\right)\ \forall\left(V,h,m\right)|_{m=\phi(V,h)} \in L$. This last simplification is made possible by the fact that neither f_h nor f_m vanishes on the fold lines and hence, by continuity, in a neighborhood of those lines.[1]. In fact, we have that: f is linear with respect to h; m has been substituted by a function of V and h which is, of course, still linear on h; and $f_h \neq 0$ on the fold lines. Then we can divide by f_h, obtaining the expression for h in all points of F.

More generally, this is permitted by the condition claimed in 5.10 for the folded points, i.e.

$$D_{(h,m)}f(p) \text{ has full rank}$$

This condition is obviously weaker then the condition $f_h \neq 0$ supposed before since now we can accept that f_h vanishes when f_m does not. Anyway this is not really important in our model since, even if f_h would vanish somewhere on a fold line, linearity in both – m and h – permits us to locally invert $h = \phi\left(V,m\right)$ and then divide by f_m in place of f_h. Then for our system the two conditions are equivalent, up to this simple expedient.

This one, and the other condition $\partial^2 f(p)/\partial V^2 \neq 0$, are obviously verified looking to Figure 7.4, where the folded surface S appears sufficiently regular to satisfy them.

With all those conditions satisfied, we can apply GSPT to the system 7.4 without any other hesitation.

[1] A more detailed analysis refering to this and the following conditions was done in appendix E. There, we have remarked that this regularity is not just local: it is true for all the points of S in the range of evolution of the system i.e. for $V \in (-70, 0)$.

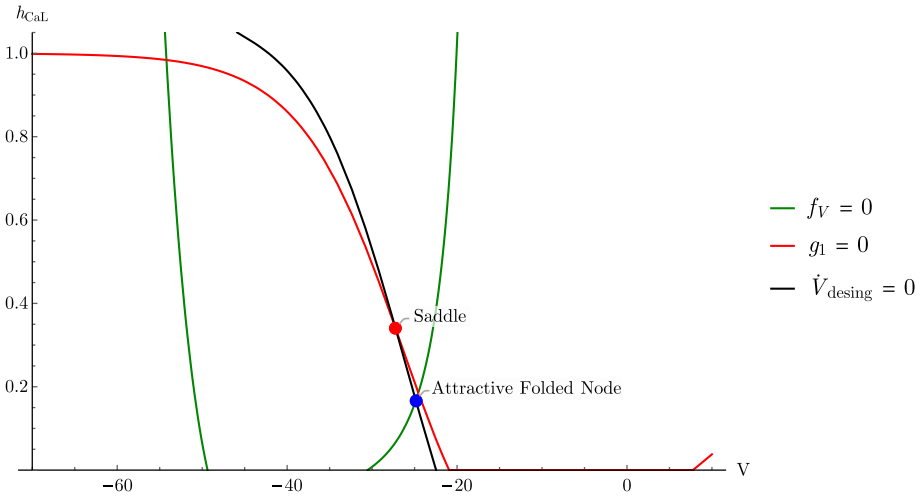

Figure 7.3: Fold lines are plotted in green. The other two equations for the research of the equilibria are plotted too. The two big points are the singularities of the system, determined by the intersections of the previous equations: the blue one is a fold singularity while the red one is the ordinary one. Everything was calculated using default parameters and $g_{KV} = 0.05$; $nS/pF, \tau_{mhERG} = 100\ ms$.

First of all, let us proceed with the analysis by looking to the equilibria of system 7.4 in the limit case when $\epsilon \to 0$. By performing a numerical computation we found two singularities: an attractive folded node and a saddle. Of course, as it was said in chapter 5, in order to do that we had to project the system on the (V, h_{CaL})–plane and desingularize it, finding the slow desingularized problem of the form of 5.9:

$$\begin{aligned} \dot{V} &= \dot{V}_{desing} \\ \dot{h} &= -f_V g_1 \end{aligned} \Bigg|_{m=\phi(V,h)} \tag{7.6}$$

where $\dot{V}_{desing} = f_h g_1 + f_m g_2$.

This system has three equilibria at points where $\dot{V}_{desing} = 0$ and at least one of f_V and g_1 is vanishing. Only two of them are plotted since the third one is out of the range of $h \in (0, 1)$; anyway it is a folded focus then it is of no interest for the analysis of canards and for the dynamics of the system.

As stated before the saddle is a real equilibrium of system 7.4 since it is not on the fold and $g_1 = 0$ (and $g_2 = 0$ too, see section 5.2). On the other hand, the attractive folded node lies on one of the fold lines and therefore represents the point where the trajectories go from the attractive manifold S_a to the repelling one S_r (see Figure 7.3).

In the next sections we found and studied singular canards of the system and then maximal canards emerging on the general case where $\epsilon > 0$. Before doing that, let us see a 3d representation of the folded surface with those singular points and a simulation of the system: MMOs composed by SAOs and a global return mechanism (given by the LAO). All these objects are plotted (Figure 7.4) for $g_{KV} = 0.05\, nS/pF$ and default parameters.

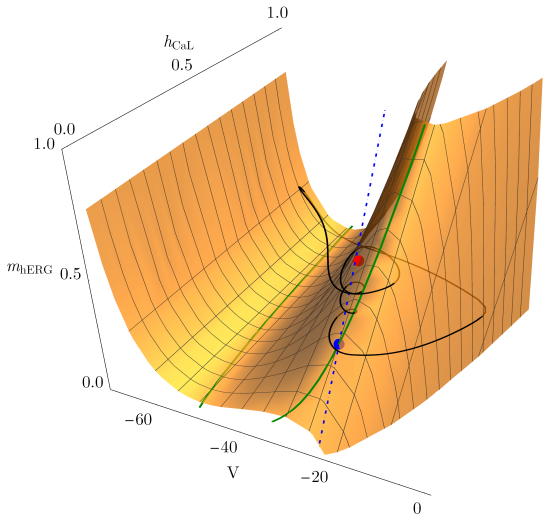

Figure 7.4: Slow manifold S with its fold lines (green). The folded node (blue) and the saddle (red) with a simulation (black) that shows small oscillations starting near the folded node and relaxtion oscillations after having approached the other fold line ($g_{KV} = 0.05\,nS/pF$ and default parameters). The simulation is turning around the weak canard (dashed blue line[3]) but we will talk about this in the next section.

7.3 Singular Canards

The next step of this study is the computation of singular canards. Remembering once more what we stated in chapter 5, singular canards are determined by the eigenvectors directions of the folded node. Thanks to this calculation, we are able to show a representation of singular canards and the consequent funnel (shadowed gray region) limited by the strong singular canard and the fold line on the attractive manifold S_a (see Figure 7.5).

In Figure 7.6 we can also observe the simulation previously computed in Figure 7.4 projected onto the 2d-plane (V, h_{CaL}): we can see that it enters the funnel and starts oscillating around the weak singular canard passing through the folded node. After a few oscillations the system is attracted by the saddle equilibrium and then pushed away from it following the eigendirection relative to its "strong" eigenvalue (i.e. the greater eigenvalue in absolute value). Finally the LAO permits the global return mechanism to occur and then the system can repeat the cycle.

In order to better visualize that the oscillations of the simulation turn around the weak canard, in Figure 7.7 g_{KV} was reduced to the value $0.01\,nS/pF$ and τ_m was increased to the value $200\,ms$: as it was expected in Figure 7.7/d SAOs rotate around the weak singular canard for a while, until they are attracted from the saddle equilibrium of the system in Figure 7.7/c.

[3] This line has been extended to 3 dimensions calculating a point in the vicinity of the folded node belonging to the 2d-eigenvector and therefore by continuity it is supposed to belong to the folded surface S too. Thanks to the invertibility seen before, we can reobtain the third coordinate of that point.

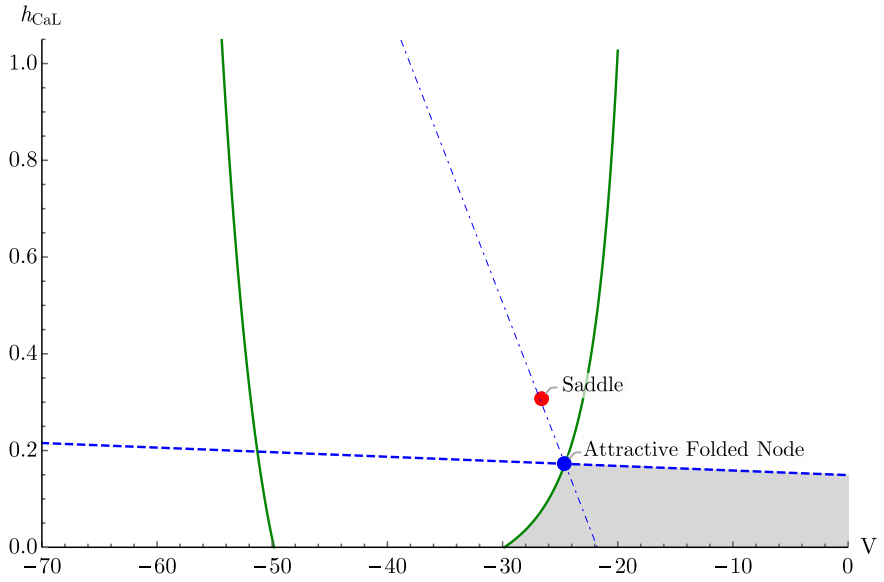

Figure 7.5: Fold lines are plotted in green. The two big points are the singularities of the system: the blue one is a fold singularity while the red one is the ordinary one. Singular canards are plotted using dashed thicked lines (for the strong $\tilde{\gamma}_s$) and dot-dashed lines (relative to the $\tilde{\gamma}_w$). Everything was calculated using default parameters and $g_{KV} = 0.05$; $nS/pF, \tau_{mhERG} = 100\ ms$.

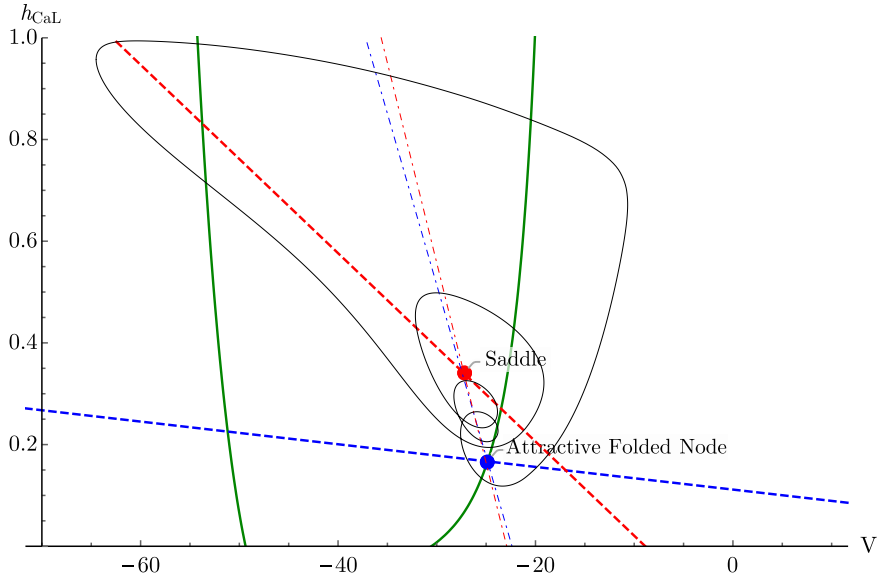

Figure 7.6: Replot of Figure 7.5 with the previous simulation: SAOs rotate around the eigenvector direction associated to the smallest eigenvalue, hence around the weak canard. This time the eigenvectors direction at both singularities are plotted, keeping the respective colours, and using dashed thicked and dot-dashed lines for strong and weak eigenvectors.

The same rotations obviously occur not only in the 2d-section, but also in the original 3d-space. The maximal weak canard and the simulation with $g_{KV} = 0.05\ nS/pF$ and $\tau_{mhERG} = 100\ ms$ were shown in Figure 7.4: in a 3d plot it is more difficult to remark that the simulation actually rotates around this canard, but it still holds.

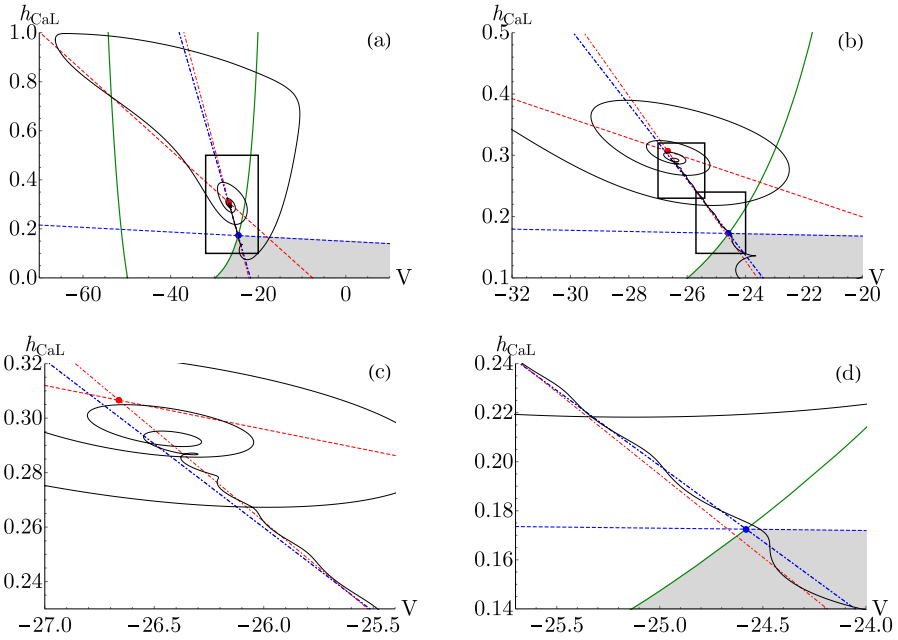

Figure 7.7: Replot of Figure 7.5 with $g_{KV} = 0.01\ nS/pF, \tau_{mhERG} = 200\ ms$ and simulation. Rectangles refer to the zoom applied in the following figure of the grid. The zoomed graphs help to better visualize the rotations around the weak singular canard.

7.4 Maximal Canards

From Equation 5.14 we know that the eigenvalue ratio $\mu := \sigma_s/\sigma_w$ at the folded node is a crucial quantity that controls the maximal number of oscillations S_{max}. More generally it determines the dynamics in the neighborhood of the folded node, since the direction of the flow and the amplitude of those oscillations are influenced too [26].

The ratio μ is linked to S_{max} thanks to the existence of secondary canards. Before talking about this object, let us focus on the number of SAOs computationally calculated and the maximal number predicted by the already cited Equation 5.14. The result is plotted in Figure 7.8 for different values of τ_m by increasing g_{KV} until no more oscillations are found. We can observe that S_{max} (denoted by red points) actually always overcomes the number of calculated oscillations (plotted in blue), as it was expected. Those oscillations were calculated on the limit cycle of the system evolved with that parameter, counting the number of peaks all along a period evolution of V. The first peak was not taken into account since it is the one that allow the return mechanism, i.e. it is

the LAO.

By the way, not all the oscillations has been calculated, otherwise blue and red points of Figure 5.3 would coincide. This is due to the fact that we just explained: those oscillations are calculated on the limit cycle. Let us better understand why this is a critical issue.

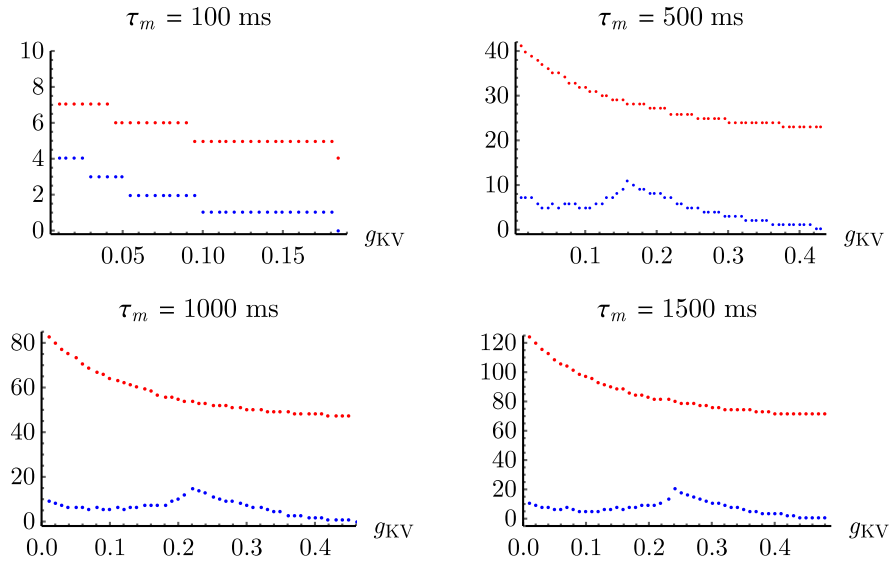

Figure 7.8: Red points denote the maximal number of secondary canards calculated thanks to the formula 5.14; blue points denote the number of SAOs computationaly calculated. Both plotted as function of g_{KV} varying τ_{mhERG} as indicated in title of every element of the grid.

As we said in chapter 5 secondary canards split the funnel – more precisely they split the sector of secondary canards – in subsectors (remember Figure 5.3). When the solution of the system enters the funnel, it enters in one of these specific subsectors, which are determined by the maximal canards, primary and secondary altogether.

We suppose to have $k = S_{max}$ secondary canards and we denote the i^{th} secondary canard with ξ_i for $i = 1, \ldots, k$, the primary strong canard with $\gamma_s = \xi_0$ and the primary weak canard with $\gamma_w = \xi_{k+1}$. If we consider a solution which enters the funnel in the subsector limited by ξ_i and ξ_{i+1} then the simulation will accomplish i rotations around the weak canard for every $i = 0, \cdots, k$, hence it will produce i SAOs [26].

Then it is important to determine the position of these canards and verify that the number of oscillations performed actually increases when the solutions enter in the following subsector. This would grants us that canard-generated MMOs actually lead the dynamics of the 3d-system studied and therefore the similar dynamics of the initial 8d-model.

We already know from chapter 5 that, geometrically, maximal canards appear in the vicinity of a folded node as the intersection of $S_{a,\epsilon}$ and $S_{r,\epsilon}$. Therefore, in general, these manifolds intersect each other to form a curve that in the neighborhood of the folded node. Hence, in order to make the visualization

more intuitive and the construction simpler, we decided to look for maximal canards (i.e. these intersections) constrained to a plane Σ_{fn} which passes through the folded node and is transverse to the fold line F.

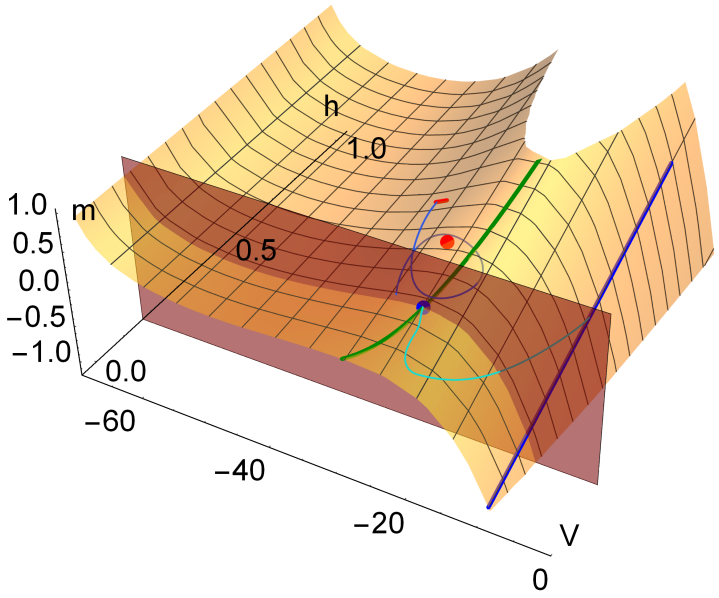

Figure 7.9: Folded surface S with the fold line F in green, the folded node p^* (blue dot) and the saddle (red dot). The blue line was chosen in order to evolve its points until they reach the plane Σ_{fn} transversal to F in p^*. Analogously, points of the red line are pushed back to Σ_{fn}. As an example, one simulation starting from each line is calculated until it touches the plane in the vicinity of p^*.

In order to find these intersections onto Σ_{fn} we had to choose a line parallel to F on S_a called L_a (plotted in blue in Figure 7.9) and a line transverse to F on S_r called L_r (plotted in red). This approach is used in [26] where Desroches et al. propose to find those intersections of the slow manifolds by defining a Boundary Value Problem (BVP).

Then, in order to calculate $S_{a,\epsilon}$ constrained onto Σ_{fn}, we built a problem that takes initial values in L_a and stops in Σ_{fn}. Through temporal evolution those points get immediately out of S_a and proceed following the slow flow along $S_{a,\epsilon}$ until it falls on Σ_{fn}.

Analogously, we took a problem which starts from Σ_{fn} with final values on L_r. Through temporal backward evolution we can repeat the same process done for L_a and find $S_{r,\epsilon}$ too.

Remark 6. Both, L_a and L_r, have to be taken sufficiently near to the fold line F, otherwise we could risk that their evolution does not follow the slow flow.

The results of this numerical calculation are plotted in Figure 7.10 where the blue curve represents the slow perturbed attracting manifold $S_{a,\epsilon}$ and the red curve represents the repelling one. Their intersections, i.e. maximal canards, can be easily identified and counted, thanks to the zoomed plot too (see Figure 7.11).

A second plot of these intersections was done in Figure 7.12 where we counted the number of SAOs occuring at each of the points of the first figure that permitted this construction. For this figure there was a computational problem similar to that of Figure 7.8: after having reached the threshold of 6 SAOs the calculator is unable to perceive the peaks, since they probably become too flat. Then even after ξ_5 only few solutions are coloured in red, i.e. recognized as performing 6 SAOs.

This is not really a problem since canards were found in previous figures from the intersection between $S_{a,\epsilon}$ and $S_{r,\epsilon}$ and we know that the number of SAOs is growing even if we are not capable of measure it.

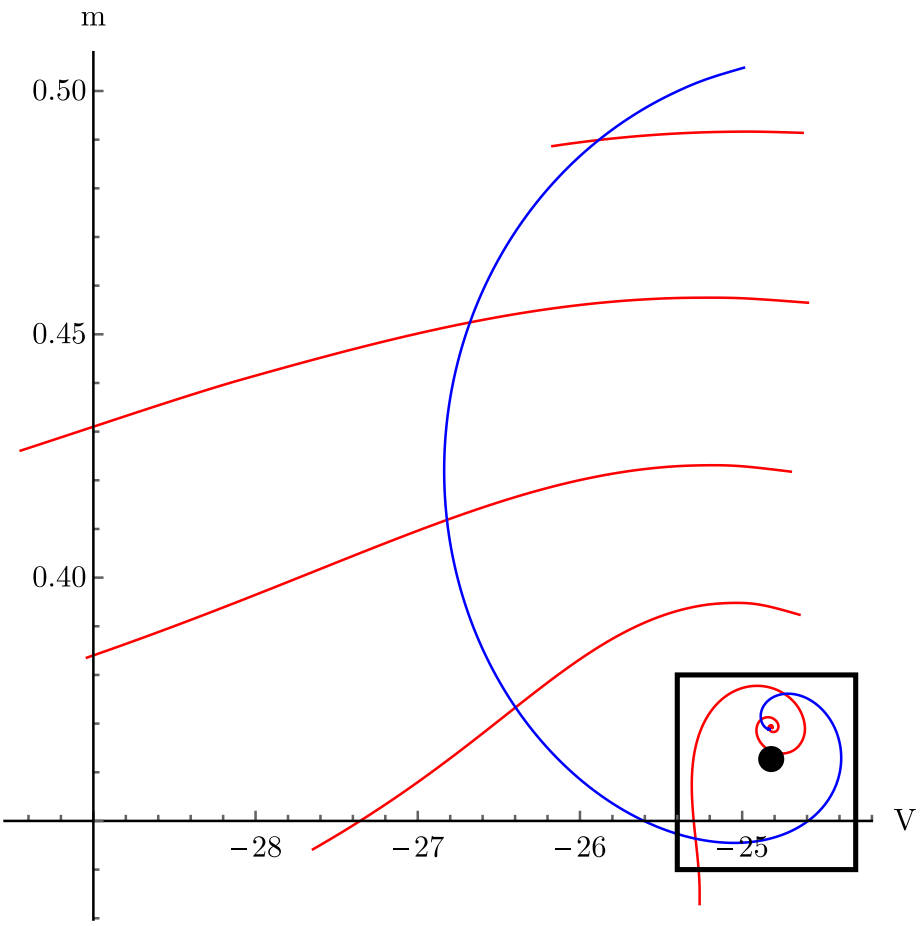

Figure 7.10: Section on the plane Σ_{fn} of the attracting (blue curve) and repelling (red curve) sheets obtained for $g_{KV} = 0.04\ nS/pF, \tau_m = 100\ ms$ and default parameters from Table 2.1. The black rectangle delimits the zoomed region of Figure 7.11. The black dot is the folded node: rotations occur around a point in an ϵ range from it.

Looking to Figure 7.8 we can remark that, for $g_{KV} = 0.04\ nS/pF$ and $\tau_m = 100\ ms$, we should find 7 secondary canards, which means 9 intersections of the slow perturbed manifolds. Unfortunately, we were able to find only 8 of

these intersections: starting from the upper one – around of $m = 0.49$, which is the strong canard $\gamma_s = \xi_0$ – and following the blue curve $S_{a,\epsilon} \cap \Sigma_{fn}$ until ξ_7. The maximal weak canard $\gamma_w = \xi_8$ was not found but clearly in Figure 7.11 the red spiral continue to turn after the blue has stopped. Then probably the starting points of L_a were not sufficient to plot all the evolved curve onto Σ_{fn}.

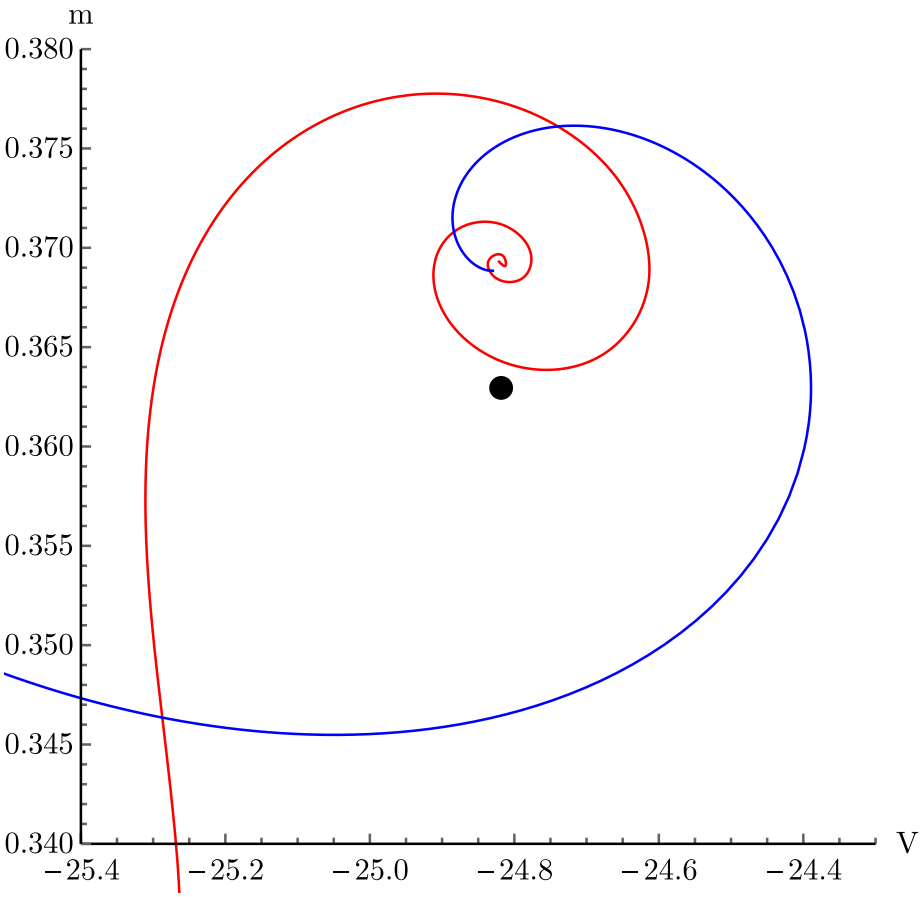

Figure 7.11: Zoom of Figure 7.10 into its black rectangle.

Another question mark on the evolution of the chosen L_a onto the plane Σ_{fn} is given in Figure 7.12: we can remark that when the points of $S_{r,\epsilon}$ crosses those of $S_{a,\epsilon}$ they actually change of colour, as expected; in the meanwhile the points of $S_{a,\epsilon}$ change a little bit "earlier", in the sense that the first SAO seems to appear before entering the sector determined by the strong canard γ_s and the first secondary canard ξ_1. This cannot be a computational error like the previos ones, since we count more SAOs than there actually are.

In conclusion, the absence of the last intersection determining the maximal weak canard and this anticipated increasing of SAOs let us suspect about the accuracy of the choice for L_a. Other choices for L_a were tried but no meaningful ameliorations were found for the moment.

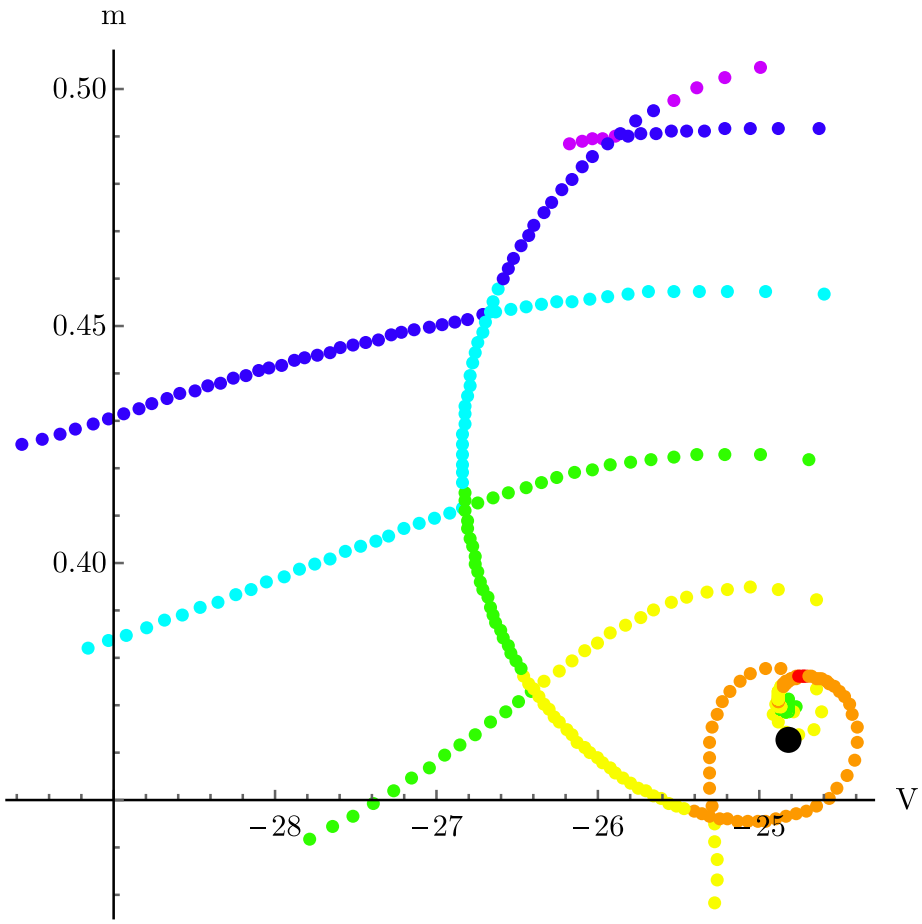

Figure 7.12: Punctual replot of Figure 7.10 with dotted colours. Those colours change progressively from purple to red and they represents the number of SAOs occured for the simulation passing through that specific point. Purple corresponds to 0 SAOs, red to 6.

Chapter 8

Conclusions

Even though this elaborate is a rather theorical work, it was almost my first real approach to applied mathematics, and absolutely the first one compeeding on biology and medecine. I truthfully enjoyed reading some chapters or paragraphs of some biologic books and confronting my friends who study those disciplines, in order to construct and improve my knowledges about cytology. Of course, I studied it partially, but I loved this melting of sciences and hope that – in the future – I will have the opportunity to work with this and many sciences, from a mathematical point of view and maybe in an even more applied environment.

Let us finally resume rapidly the work and the results that were done during the elaboration of this thesis project.

First of all, I studied the model suggested in [1], which aims to represent the dynamics of β-cells. The previously cited studies in cytology permitted me to roughly understand the idea behind this construction.

Next, I started learning how to use XPPAUT: it is a general numerical tool for simulating animating and analyzing dynamical systems developped by the University of Pittsburgh; it also includes a frontend to a continuation and bifurcation package called AUTO. At the beginning we thought about using this tool in order to analyze our system and study its bifurcation. Unfortunately, bifurcation analysis is quite complicated and we were not able to fully exploit XPPAUT potential. Hence I decided to totally implement the system with *Wolfram Mathematica* since I am much more confortable with Wolfram language. This thesis let me also improve my skills on the use of this last tool[1].

The analysis of the fast-slow model made in chapter 4 let us detect its three different behaviours and a particular attention was devoted to bursting activity: ascertain the appearance of MMOs was of the main importance in this work. Furthermore, these oscillations were seen to be related to the birth of the mathematical objects called *canards* (chapter 7), as a result of the rotation of the solution around the weak canard in the vicinity of a folded node[2]. The maximal number of SAOs has been predicted thanks to Equation 5.14 and this prediction happens to be coherent with the number of intersections obtained in Figure 7.10. Finally, the number of oscillations performed by a particular solu-

[1] Of course all the notebooks are available to the reader: do not hesitate to contact me on simone.battaglin@gmail.com.

[2] See Figure 7.7.

tion is expected to depend on the specific subsector where the simulation enters the funnel and this statement was almost perfectly verified in Figure 7.12 by computing that the number of SAOs increments at each crossing of a secondary canard.

8.1 Suggestion for Future Developments

In the future this work could be improved in different ways.

First of all, we could try to solve the technical problems appeared in the end of the last chapter by better understanding, for example, how L_a and L_r should be taken in order to succed in counting all the intersections. A 3d representation of the evolution of these curves could be shown too, for the purposes of a better visualisation.

Second, other parameters could be changed, trying to look for similar behaviour or the appearance of other phenomena, which were not expected in our case. Even the choices taken in order to reduce the initial system to a 3-dimensional one could be reinvented. Some changes were frequently tried in the last months without finding much interesting cases, but other approaches can still be tried.

Lastly, the 3d-model could be thought as a slow-medium-fast system, and not only a slow-fast like we did. In fact, values found in 7.3 could be interpreted as splitting the system in two, but also in three, time scales. In the last weeks of work I studied this possibile variation, but no interesting dynamics were found. Therefore more work will be necessary to adapt the system to three different time scales.

Appendix A

Fenichel Theorem

Theorem A.1 (Fenichel Theorem)**.** *Suppose $M = S_0$ is a compact normally hyperbolic submanifold of the critical manifold S of 5.1. Let $f, g_1, g_2 \in \mathscr{C}^r, r < \infty$. Then for $\epsilon > 0$ sufficiently small the following hold:*

(F1) *There exists a locally invariant manifold M_ϵ diffeomorphic to M. Local invariance means that M_ϵ can have boundaries through which trajectories enter or leave.*

(F2) *M_ϵ has a Hausdorff distance of $O(\epsilon)$ from M.*

(F3) *The flow on M_ϵ converges to the slow flow as $\epsilon \to 0$.*

(F4) *M_ϵ is $\mathscr{C}^r$-smooth.*

(F5) *M_ϵ is normally hyperbolic and has the same stability properties with respect to the fast variables as M (attracting, repelling or saddle-type).*

(F6) *M_ϵ is usually not unique. In regions that remain at a fixed distance from the boundary of M_ϵ, all manifolds satisfying* (F1-F5) *lie at a Hausdorff distance $O(\exp(-K/\epsilon))$ from each other for some $K > 0$ with $K = O(1)$.*

The normally hyperbolic manifold M has associated local stable and unstable manifolds

$$W^s_{loc}(M) = \bigcup_{p \in M} W^s_{loc}(p) \qquad W^u_{loc}(M) = \bigcup_{p \in M} W^u_{loc}(p)$$

where $W^s_{loc}(p)$ and $W^u_{loc}(p)$ are the local stable and unstable manifolds of p as a hyperbolic equilibrium of the layer equations, respectively. These manifolds also persist for $\epsilon > 0$ sufficiently small: there exist local stable and unstable manifolds $W^s_{loc}(M_\epsilon)$ and $W^u_{loc}(M_\epsilon)$, respectively, for which conclusions (F1-F6) *hold if we replace M_ϵ and M by $W^s_{loc}(M_\epsilon)$ and $W^s_{loc}(M)$ - or similarly by $W^u_{loc}(M_\epsilon)$ and $W^u_{loc}(M)$.*

We call M_ϵ a *Fenichel manifold.* Fenichel manifolds are a subclass of slow manifolds, invariant, on which the vector field has speed that tends to 0 on the fasi time scale as $\epsilon \to 0$.

Appendix B

Points Classification

In order to better understand the notation used in this thesis, let's resume quickly the classification of points in $\mathbb{R}^3$ with a slow folded surface S done by Benoît in [8]. This classification is made simply following the dynamic at that point P i.e. looking to the flow at P.

We remember that we are considering the fast-slow system 5.1:

$$\begin{aligned} \epsilon\dot{x} &= f(x,y,z) \\ \dot{y} &= g_1(x,y,z) \\ \dot{z} &= g_2(x,y,z) \end{aligned}$$

and that the slow surface S and the fold L are definied by 5.5 and 5.7 respectively:

$$\begin{aligned} S &:= \{(x,y,z) : f(x,y,z) = 0\} \\ L &:= \{(x,y,z) \in S : f_x(x,y,z) = 0, f_{xx}(x,y,z) \neq 0\} \end{aligned}$$

There are five main types of points. A point $P \in \mathbb{R}^3$ can be a:

- P is a *rapid point* if $P \notin S$
- P is a *slow point* if $P \in S \setminus L$; in that case it can be:
  - *attractive* if $P \in S_a$ i.e. if $f_x(P) < 0$
  - *repulsive* if $P \in S_r$ i.e. if $f_x(P) > 0$
  - *singular for 5.4* if f, g_1, g_2 vanish together (which is of no interest and does not happen in this work)
- $P \in L$ is a "regular" *folded point* if $(f_x g_1 + f_y g_2) f_{xx}|_P \neq 0$; it will be *attractive* or *repulsive* depending on the sign of this last term, as for previous type
- $P \in L$ is a *"fronce" point* - which can maybe be translated by "gathered" - if $f_{xx}(P) = 0$
- $P \in L$ is a *pseudo-singular point* if $f_x g_1 + f_y g_2|_P = 0$

Points that are interesting in canard generation are pseudo-singular points, in particular folded nodes. That is why they are interesting for us and they were treated in section 5.2.

A graphical visualisation for every type of point can be found in [8] but it was not considered necessary since the points that are inspected were well visualised in the previous pages. In order to simplify the comparison I chose to follow the same order as Benoît.

Appendix C

Time Delay $\tau_{\mathbf{m_{KV}}}(\mathbf{V})$

As stated in chapter 2 the delayed rectifying potassium channels were assumed to activate on a voltage-dependent timescale:

$$\tau_{mKV} = \begin{cases} \tau_{mKV,0} + 10 \exp\left(\min\left(Log_e(3), -\frac{V+20\,mV}{6\,mV}\right)\right) & \text{if } V < 26.6\ mV \\ \tau_{mKV,0} + 30\ ms & \text{otherwise} \end{cases} \tag{C.1}$$

This implies that τ_{mKV} is constantly equal to 32 ms for $V > 26.6$ and $V < -(20+6Log_e(3)) \approx -26.6$; between this two values τ_{mKV} follows a negative exponential trend (Figure C.1).

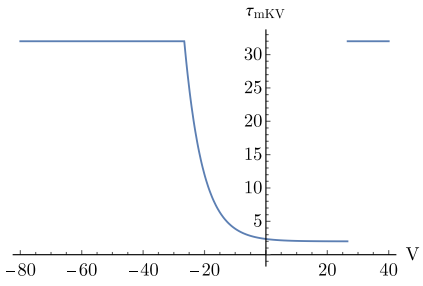

Figure C.1: Plot of τ_{mKV} with respect to V with default parameters. Let us remark that the parameters used to define this function were never changed during this paper.

Discontinuity does not cause troubles since the membrane potential never reaches 20 mV.

Appendix D

Numerical Fitting for Fast Variables

Here we will refer to Figure 6.7 and verify the intuition of the approximation which has been made for fastest variables in chapter 6.

Numerical data obtained thanks to two type of simulations were fitted with non-linear algorithm Levenberg-Marquardt. Other algorithms, such as Gauss-Newton or conjugate gradient, were tried too but no significantly better results were found.

The aim was to approximate these three variables $\{h_{Na}, h_{CaT}, m_{BK}\}$ with their steady-state functions, which are three Boltzmann functions. Therefore I chose a generic Boltzmann function:

$$\left(1 + \exp\left(\frac{V - a}{b}\right)\right)^{-1}$$

to interpolate simulated data.

Resulting parameters obtained from this interpolation were shown in Table D.1 with $a = V_x$, $b = n_x$ with the committed standard error for every variable.

In Figure D.1 we can see a plot of simulations, steady-state functions and interpolated Boltzmann functions related to the parameters in Table D.1 for each of the three variables during spiking ($g_{KV} = 1\ nS/pF$) and bursting ($g_{KV} = 0.2\ nS/pF$) activity.

Finally we can assume that the standard errrors obtained are acceptable and therefore that variables $\{h_{Na}, h_{CaT}, m_{BK}\}$ are quite well approximated by their steady-state functions $\{h_{Na,\infty}(V), h_{CaT,\infty}(V), m_{BK,\infty}(V)\}$ respectively.

Var	Param	SS fct	Spiking		Bursting	
			Estimate	St. Err.	Estimate	St. Err.
h_{CaT}	V_x	64	64.6459	0.2057	64.2214	0.1006
	n_x	8	9.2094	0.2833	8.1816	0.1095
h_{Na}	V_x	42	41.6071	0.2472	42.0782	0.0551
	n_x	6	6.4200	0.1782	5.9900	0.0388
m_{BK}	V_x	0	−8.9728	1.2104	−5.3059	0.5625
	$-n_x$	10	13.1754	0.5087	12.2707	0.2513

Table D.1: Parameters for the steady-state functions of h_{Na}, h_{CaT}, m_{BK} and the fitting Boltzmann functions based on simulations in the spiking and bursting case calculated with Levenberg–Marquardt algorithm with *Wolfram Mathematica*. Respective standard error is shown too.

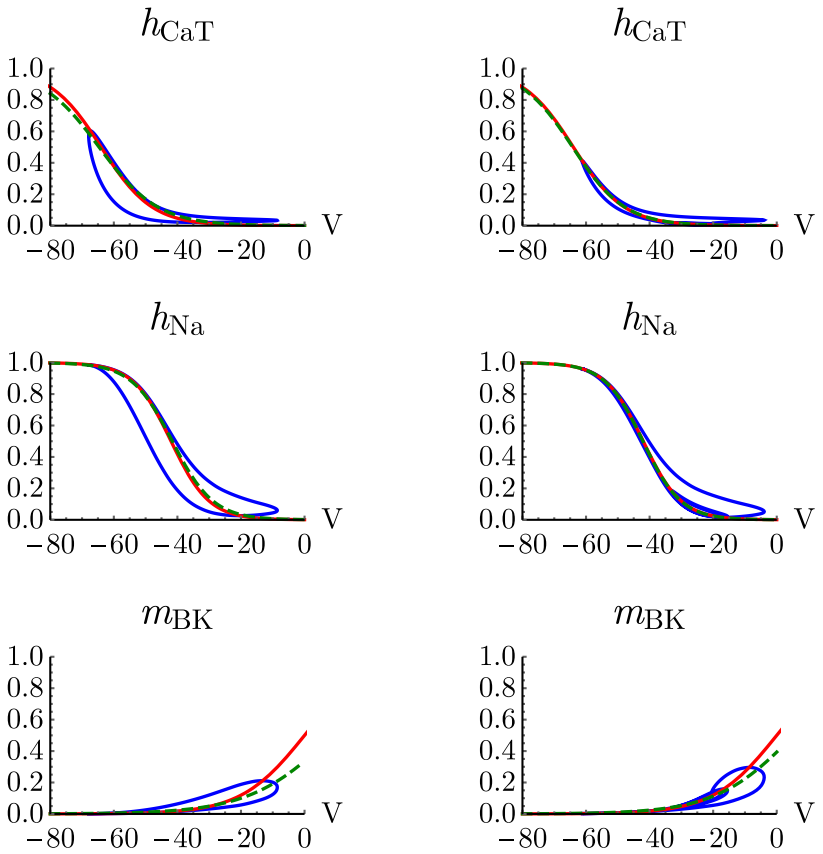

Figure D.1: Plot of steady-state functions (red curves) for the three fast variables indicated in the figure. On the left side we simulate the spiking activity (blue cycles) with default parameters from Table 2.1 and fit them with a Boltzmann function (dashed green curves). On the right side the same thing was done for bursting activity ($g_{KV} = 0.2\ nS/pF$)

Appendix E

Conditions on the Fold Points

The aim of this appendix is to verify the assumptions made on 5.10, i.e.:

$$\frac{\partial^2 f}{\partial V^2}(p) \neq 0 \quad \text{and} \quad D_{(h,m)}f(p) \text{ has full rank} \tag{E.1}$$

for every $p \in L$.

As we claimed in chapter 7 the function f of the system 7.5 is linear with respect to h and m, hence we are able to write it such as:

$$f(V,h,m) = \alpha(V) + h\beta(V) + m\gamma(V) \tag{E.2}$$

Then we have:

$$\begin{aligned} f_V(V,h,m) &= a(V) + hb(V) + mc(V) \\ f_h(V,h,m) &= \beta(V) \\ f_m(V,h,m) &= \gamma(V) \end{aligned}$$

where a, b, c are the derivative of α, β and γ respectively.

We have already seen in chapter 7 that the second condition of E.1 is equivalent to ask that β and γ do not vanish together. Anyway we will see that on the fold lines they do not vanish at all.

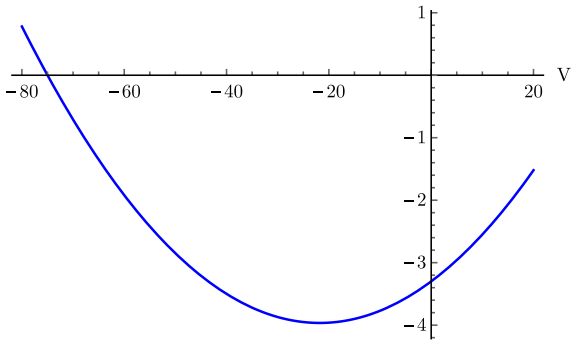

Figure E.1: Plot of the function $\gamma(V)$ in $(-80, 20)$.

In the 3d model we simply have:

$$\gamma(V) = -g_{hERG}(0.22 - 0.007V)(V - V_K)$$

where $g_{hERG} = 0.2$ and $V_K = -75$. Then $\gamma(V)$ will vanish only for $V = -75$ and $V > 30$, and both of these values are of no interest for us since V will never reach those values in the folds (nor in the simulations of the system). The function $\gamma(V)$ is shown in Figure E.1.

The function $\beta(V)$ has a more complex form, which is not interesting to be written and depends on g_{KV}, therefore its own expression vary in the different cases we have studied. Anyway the reasoning is not very different: β also has two zeros, one always positive disappears rapidly by increasing g_{KV}, the other one will always be less than -75. The function $\beta(V)$ is shown in Figure E.2.

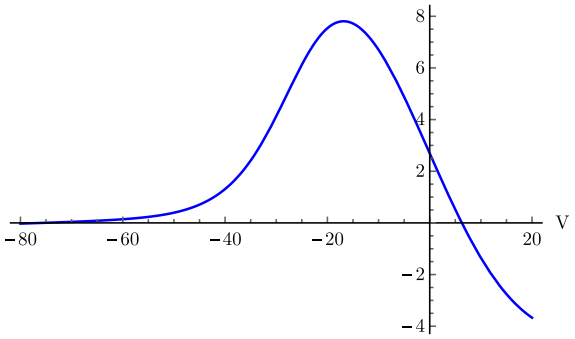

Figure E.2: Plot of the function $\beta(V)$ in $(-80, 20)$ with $g_{KV} = 0.05\,nS/pF$.

Relatively to the first condition of Equation E.1, the second derivative was calculated only onto the points of the fold lines. In fact since the surface is folded with respect to V, there is no doubt that this derivative will vanish somewhere. It is important that it does not happen on the fold lines.

In Figure E.3 we can observe all this and also what we were saying a few lines ago i.e. the fold lines are contained between the following intervals in V: $(-60, -45)$ and $(-35, -20)$. Therefore none of β and γ will vanish on them neither.

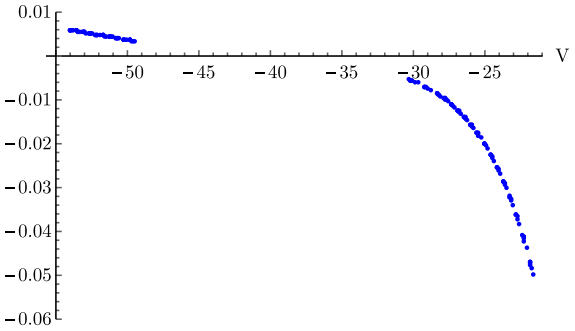

Figure E.3: $\frac{\partial^2 f}{\partial V^2}$ on the points of the fold lines with $g_{KV} = 0.05\,nS/pF$.

Bibliography

[1] Morten Gram Pedersen. A biophysical model of electrical activity in human β-cells. *Biophysical Journal*, 99, 2010.

[2] Bruce Alberts, Dennis Bray, Julian Lewis, Martin Raff, Keith Roberts, and James D. Watson. *Molecular Biology of the Cell.* Garland Science, 3 edition, 1994.

[3] M. Braun, R. Ramracheya, J. Karanauskaite, C.J. Partridge, P.R. Johnson, and P. Rorsman. Voltage-gated ion channels in human pancreatic β-cells: electrophysiological characterisation and involvement in insulin secretion. *Diabetic Medecine*, 24, 2007.

[4] Christopher Fall, Eric Marland, John Wagner, and John Tyson. *Computational Cell Biology.* Springer, 2005.

[5] Barbara Rosati, Piero Marchetti, Olivia Crociani, Marzia Lecchi, Roberto Lupi, Annarosa Arcangeli, Massimo Olivotto, and Enzo Wanke. Glucose- and arginine-induced insulin secretion by human pancreatic β-cells: the role of hERG K^+ channels in firing and release. *The FASEB Journal*, 14, 2000.

[6] Theodore Vo, Richard Bertram, Joel Tabak, and Martin Wechselberger. Mixed mode oscillations as a mechanism for pseudo-plateau bursting. *Journal of Computational Neuroscience*, 28, 2010.

[7] A. M. Scott, I. Atwater, and E. Rojas. A method for the simultaneous measurement of insulin release and β-cell membrane potential in single mouse islets of Langerhans. *Diabetologia*, 21, 1981.

[8] Eric Benoît. Systèmes lents-rapides dans $\mathbb{R}^3$ et leurs canards. *Société Mathématiques de France, Astérisque*, 1983.

[9] M. Desroches, J. Guckenheimer, B. Krauskopf, C. Kuehn, H. Osinga, and M. Wechselberger. Mixed-mode oscillations with multiple time scales. *SIAM Review*, 54, 2012.

[10] Morten Brøns, Martin Krupa, and Martin Wechselberger. Mixed mode oscillations due to the generalized canard phenomenon. *Fields Institute Communications*, 49, 2006.

[11] A. L. Hodgkin and A. F. Huxley. A quantitative description of membrane current and its application to conduction and excitation in nerve. *The Journal of Physiology*, 117, 1952.

[12] Bertil Hille. *Ion Channels of Excitable Membranes*. Sinauer Associates, 3 edition, 2001.

[13] Michela Riz, Matthias Braun, Xichen Wu, and Morten Gram Pedersen. Inwardly rectifying Kir2.1 currents in human β-cells control electrical activity: Characterisation and mathematical modelling. *Biochemical and biophysical research communications*, 459, 2015.

[14] M Zhabotinskii. Periodic kinetics of oxidation of malonic acid in solution (study of the Belousov reaction kinetics). *Biofizika*, 9, 1964.

[15] Morten Brøns, Tasso J Kaper, and Horacio G Rotstein. Introduction to focus issue: mixed mode oscillations: experiment, computation, and analysis, 2008.

[16] Martin Krupa and Peter Szmolyan. Extending geometric singular perturbation theory to nonhyperbolic points - fold and canard points in two dimensions. *SIAM journal on mathematical analysis*, 33, 2001.

[17] Martin Wechselberger. Existence and bifurcation of canards in $\mathbb{R}^3$ in the case of a folded node. *SIAM Journal on Applied Dynamical Systems*, 4, 2005.

[18] Eric Benoît. Chasse au canard. *Collectanea Mathematica*, 32, 1981.

[19] Francine Diener and Georges Reeb. *Analyse non standard*, volume 40. Editions Hermann, 1989.

[20] Peter Szmolyan and Martin Wechselberger. Canards in $\mathbb{R}^3$. *Journal of Differential Equations*, 177, 2001.

[21] Martin Wechselberger. Extending Melnikov theory to invariant manifolds on non-compact domains. *Dynamical Systems: An International Journal*, 17, 2002.

[22] Neil Fenichel. Geometric singular perturbation theory for ordinary differential equations. *J. Diff. Eq.*, 31, 1979.

[23] Theodore Vo, Richard Bertram, and Martin Wechselberger. Multiple geometric viewpoints of mixed mode dynamics associated with pseudo-plateau bursting. *SIAM Journal on Applied Dynamical Systems*, 12, 2013.

[24] Neil Fenichel. Persistence and smoothness of invariant manifolds for flows. *Indiana Univ. Math. J.*, 21, 1972.

[25] Morris W. Hirsch, Charles Chapman Pugh, and Michael Shub. *Invariant manifolds*, volume 583. Springer, 2006.

[26] Mathieu Desroches, Bernd Krauskopf, and Hinke M Osinga. Numerical continuation of canard orbits in slow-fast dynamical systems. *Nonlinearity*, 23, 2010.

[27] Martin Krupa, Nikola Popović, and Nancy Kopell. Mixed-mode oscillations in three time-scale systems: a prototypical example. *SIAM Journal on Applied Dynamical Systems*, 7, 2008.

[28] Rodica Curtu. Singular Hopf bifurcations and mixed-mode oscillations in a two-cell inhibitory neural network. *Physica D: Nonlinear Phenomena*, 239, 2010.

[29] E.M. Izhikevich. *Dynamical systems in neuroscience: the geometry of excitability and bursting*, volume 25. 2007.

[30] V. I. Krinsky and Iu M. Kokoz. Analysis of the equations of excitable membranes.-I. Reduction of the Hodgkins-Huxley equations to a 2nd order system. *Biofizika*, 18, 1973.